Homeostatic bidirectional plasticity in Upbound and Downbound micromodules of the olivocerebellar system

Elías M. Fernández Santoro[1], Lennart P.L. Landsmeer[1,2], Said Hamdioui[2], Christos Strydis[1,2], Chris I. De Zeeuw[1,3], Aleksandra Badura[1] and Mario Negrello[1*]

[1] Department of Neuroscience, Erasmus MC, Rotterdam, The Netherlands

[2] Quantum & Computer Engineering Department, Delft University of Technology, Delft, The Netherlands

[3] Netherlands Institute for Neuroscience, Royal Academy of Arts and Sciences, Amsterdam, The Netherlands

*Correspondence:

Mario Negrello (m.negrello@erasmusmc.nl)

Department of Neuroscience, Erasmus MC

Wytemaweg 80, 3015 CN Rotterdam

tel: 0031-(0)10 7043589

Abstract

Olivocerebellar learning is highly adaptable, unfolding over minutes to weeks depending on the task. However, the stabilizing mechanisms of the synaptic dynamics necessary for ongoing learning remain unclear. We constructed a model to examine plasticity dynamics under stochastic input and investigate the impact of inferior olive (IO) reverberations on Purkinje cell (PCs) activity and synaptic plasticity. We explored Upbound and Downbound cerebellar micromodules, which are organized loops of IO neurons, cerebellar nuclei neurons and microzones of PCs characterized by their unique molecular profiles and different levels of baseline firing. Our findings show synaptic weight convergence followed by stability of synaptic weights. In line with their relatively low and high intrinsic firing, we observed that Upbound and Downbound PCs have a propensity for potentiation and depression, respectively, with both PC types reaching stability at differential levels of overall strength of their parallel-fiber (PF) inputs. The oscillations and coupling of IO neurons participating in the Upbound and Downbound modules determine at which frequency band PFs can be stabilized optimally. Our results indicate that specific frequency components drive IO resonance and synchronicity, which, in turn, regulate temporal patterning across Upbound and Downbound zones, orchestrating their plasticity dynamics.

Author Summary

The olivocerebellar system is a part of the brain that facilitates learning and controlling movements. To coordinate movements it integrates sensorimotor information with motor command signals. The resulting behaviour needs to be continuously adjusted during motor learning. The leading hypothesis is that changes in strength of the synaptic connections between neurons underlie the learning process. The challenge is to elucidate the factors that determine the exact timing and precision of the learned movements. To answer this question we developed a computational model of the two main types of modules of the olivocerebellar system that can control different types of movements in a bidirectional fashion. We found that the rhythm and coupling of the olivary neurons play an important role in controlling and stabilizing plasticity in the cerebellar cortex of both types of modules, together shaping learning-dependent timing of motor behaviour.

Introduction

Procedural learning is an ongoing process that requires continuous adjustment and maintenance of incoming sensory input and resulting motor actions. Accordingly, like most other networks in the brain, sensorimotor control systems engage recurrent circuits with feedback capabilities, leveraging neuronal plasticity mechanisms that depend on the activity of synapses [1–3]. The olivocerebellar loop is one of the prime examples of a sensorimotor circuit where the dominant plasticity mechanisms are determined by incoming sensory and motor signals [4]. The olivocerebellar loop consists of the cerebellar cortex (CC), cerebellar nuclei (CN) and the inferior olive (IO), which feeds back into the CC via the climbing fibers (CFs) [5]. The sole output of the CC is generated by the inhibitory Purkinje cells (PCs), which receive sensorimotor information from the excitatory mossy fiber (MF) - parallel fiber (PF) pathway as well as the excitatory CF pathway.

The extensive dendritic trees of PCs receive signals from many PFs, all of which originate from granule cells [6,7]. Together with the inhibitory molecular layer interneurons, the excitatory PFs can modulate the simple spike (SSpk) activity of PCs, allowing for precise bidirectional control [8,9]. Individual PFs form relatively weak synaptic connections with PCs, [10], but as a group they can readily double the intrinsic SSpk firing frequency when needed for online sensorimotor control [11].

In contrast, in most mammals each PC receives a single CF from the IO, which delivers a powerful excitatory input resulting in an all-or-none complex spike (CSpk), [4]. Different from the SSpks (~50-100 Hz), the CSpks occur at a relatively low firing frequency (~1 Hz) during spontaneous activity and they can increase their instantaneous firing frequency about ten-fold during modulation [8]. Since the CSpks are triggered by the IO activity [12], they reflect the integration of its excitatory signals from one or more of the

ascending or descending afferent systems [13,14] and its inhibitory input signals from the hindbrain [15–18]. Interestingly, the nuclei that form the sources of the excitatory inputs to the IO are largely overlapping with the sources of the MF pathways that provide the sensorimotor signals to the CC via the PFs [19].

During learning the PF to PC synapses undergo activity-dependent changes guided by the CF signals [20]. To avoid ceiling and saturation effects [21–23], this configuration requires the PF-PC synapses to be kept in a balance by complementary, depression and potentiation mechanisms [20]. When PFs and CFs are activated in the same period, the PF to PC synapse will be depressed, a process referred to as PF to PC long-term depression (LTD; [20,24]). When PFs and CFs are activated out of phase, the PF to PC synapse will be potentiated (Long-term potentiation, LTP; [25]). Thus, even though the level of induction of depression or potentiation may vary substantially among individual PCs [26,27], for all PCs it is ultimately the moment of firing of the CF with respect to that of the MF - PF pathway that determines the changes in synaptic weights [28].

It is therefore paramount to understand which factors determine the exact timing of the IO neurons. In this respect, IO neurons are endowed with rather unique properties. They are probably more densely coupled via dendro-dendritic gap junctions than any other type of neuron in the mammalian brain [29–31] and they express high levels of voltage-gated and calcium-dependent ion-channels that allow them to oscillate at frequencies of up to 10 Hz [32–36]. In addition, olivary spines stick with their long necks into glomeruli, receiving both an excitatory and inhibitory input [37,38], which renders the excitability of these spines very sensitive to the timing between both inputs [39]. As a result, the interplay between the excitatory and inhibitory inputs to the IO as well as the temporal relation with the subthreshold oscillations (STOs) of the coupled olivary cells determines whether and when an olivary action potential will be generated [16,40–42].

Question remains how stability can be achieved in the olivocerebellar loops following procedural learning. Several studies have shown that activity-dependent synaptic plasticity is generally rather unstable in recurrent circuits [1,43,44], often leading to difficulties with network dynamics [1,23,45–48]. Solving this question for the olivocerebellar modules becomes particularly challenging when taking into account profound differences among them. Indeed, the spontaneous, intrinsic SSpk firing frequency of PCs that express Aldolase-C is significantly lower (30-90 Hz), than that of PCs that do not (60-120 Hz), [9]. These different spiking properties of the Aldolase-C positive and negative microzones come with different topographic connections of the modules involved [49–53] as well as with different propensities for the induction of plasticity at their PF to PC synapses [54]. Moreover, Aldolase-C positive and negative zones are associated with specific learning tasks that require predominantly upbound or downbound changes in SSpk activity during the training [28].

So, are there common mechanisms in the olivocerebellar system that can stabilize changes in synaptic weights across modules serving differential behaviours? We hypothesize that the resonant dynamics of the olivocerebellar loops, highlighted above, are key to stabilize PF-PC synaptic weights during procedural learning in both the Upbound and Downbound modules and thereby to establish robust encoding of learned associations between movements and the predictions of their sensory outcomes [28]. To test this hypothesis we generated a novel network model of the olivocerebellar system that does not only reverberate quasi-periodically [35,55,56], but also represents different modules with different intrinsic, electrophysiological properties of its PCs. Our simulations indicate that the upbound and downbound characteristics are not only determined and stabilized by the differences in the intrinsic neuronal activity, but also by the loop dynamics exploiting the STOs and resetting phenomena in the IO, that the whole of the synaptic weights at the PF to

PC synapse in both main types of microzones can be stabilized over multiple repeated PF inputs, that plasticity at the PF to PC synapses stabilizes the SSpk activity and CF pause, that specific PF frequency bands differentially drive plasticity, indicating that frequency components drive IO resonance, and that frequency-selectivity in turn is also shaped by the dynamics of IO gap junction coupling, as it leads to synchronized firing and phase locking. Together, our data highlight that temporal pattern selectivity processing across both Upbound and Downbound micromodules is enhanced and stabilized by reverberations in the olivocerebellar loop during procedural learning.

Results

Designing an olivocerebellar loop model to examine plasticity dynamics

Our hypothesis is that PF-PC synaptic weights are stabilized during procedural learning by the resonant dynamics of the olivocerebellar loops. Hence, we propose a model of the olivocerebellar system (**Fig. 1A**), which is decoupled from the rest of the brain to focus on the resonant network dynamics that drive plasticity. The hypotheses we tested with this model are centered on exploration of synaptic stability during ongoing plasticity. We emulated ongoing arbitrary cortical and subcortical inputs to the cerebellum via 5 uncorrelated PF bundles, which is conveyed by 100 PCs via 40 CN cells to 40 cells in the IO. These IO cells have the ability to respond by advancing or delaying their phase as a function of when inhibition arrives in the oscillation cycle, as observed in *in vivo* experiments [16,35,42,57–63].

As input to our model network we used bundles of PFs as a noisy current input rather than individual synapses. A bundle of PFs represents the combination of numerous synaptic sources, as expected during the awake and behaving state [64,65]. To avoid biasing the signal types, we modelled the background input as composed of a finite number of distinct stochastic contextual signals, via the Ornstein-Uhlenbeck (OU) process, taken to represent the integrated, continuous current from large numbers of PF EPSCs [66]. Our PF bundles can be seen as bundles of correlated input originating via MF rosettes [10,67]. Given that around 90% of PF synapses are silent [68], we modelled 5 bundles with approximately 200 active PFs each (**Fig. 1A-C**). The PF-PC synapse acts as a "meta-synapse", representing the average direction of change of the individual synaptic weights in the PF bundle. To represent plasticity, we added a weight value for each PF bundle, which could change independently. A crucial aspect of our model is that we repeated presentations of this so-called "frozen input",

to the PFs stream to test the hypothesis that under this stimulus, representing sensorimotor contingencies, there was a synaptic adjustment and weight stabilization in the PF bundles.

We tuned the PCs firing frequency to represent a mixture of their intrinsic firing frequency and their response to the PF input. As shown experimentally [9], when the PF input was completely absent, PCs had an intrinsic firing frequency that was about 20 Hz lower than when the PF input was present.

For simplicity we focussed on the primary drivers of the olivocerebellar loop dynamics - the GABAergic CN projection cells, and excluded cells involved in other loops. CN AdEx model cells were primarily designed to have robust transmission of rate coding [69]. Our CN cells received divergent input from the PC layer, which modulated CN responses in an anti-correlated fashion [69,70].

It is known that the IO has a mixture of cells: some of which oscillate robustly, some display dampened oscillations, while others that do not seem to display any resonant behavior. Cells which oscillate exhibit a low-frequency rhythm [(4-10 Hz); [35]]. Our modelled IO cells oscillated robustly around 5.8-6 Hz and were connected with electrotonic Connexin-36 synapses [35,71]. IO spiking synchrony was disrupted in absence of gap junction coupling (**Fig. S1**). Though anatomical clusterization of cells is highly plausible [72,73], here we examined a small set of cells without explicit clustering.

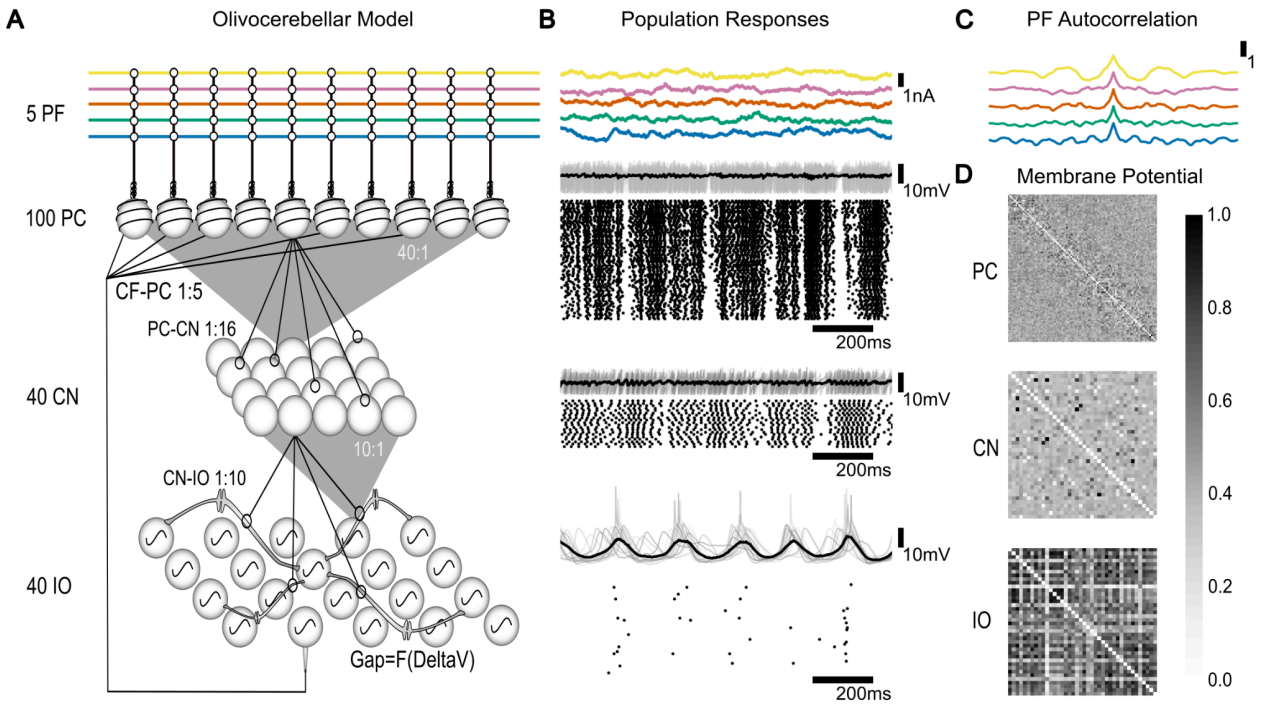

Figure 1 The olivocerebellar loop model and its population response (Downbound, coupled). (A) *Diagram of the olivocerebellar loop model. It has 5 PF bundle inputs into 100 PCs. Each PC projects to 16 CNs. The CN layer consists of 40 CN neurons, which receive input on average from 40 PCs (from 30 to 52 PCs). Each CN projects to 10 IO cells. There are 40 IO cells, each of them receiving on average 10 CNs (from 6 to 16 CNs). The IO cells are modelled with gap junctions and subthreshold oscillations. Half of the IO cells project to the PCs with each of those IO cells projecting to on average 5 PCs (from 2 to 9 cells), while each PC only receives signals from 1 IO. Each IO neuron connects to all other IO neurons in the population via the gap junctions.* ***(B)*** *From top to bottom: the PF bundle input modeled as Ornstein-Uhlenbeck processes; PC responses, CN responses and IO responses (membrane potential and raster).* ***(C)*** *Autocorrelation of each PF input. (**D**) Heatmap of the correlation of the membrane potential of each cell of each population.*

Homeostatic plasticity and CSpk-triggered LTD mechanism

To capture the essential interactions between LTP and LTD we modelled the PF-PC synapse with a mixture of a Bienenstock-Cooper-Munro-type (BCM) learning rule and a PF input dependent CSpk-triggered LTD mechanism. This CF-induced LTD operates inversely to the classical BCM mechanism and changes the probability of BCM-LTP [12]. In our model, the synaptic weights were potentiated when PC activity was low to maintain excitability. This complex combination of synaptic plasticity mechanisms enabled us to inspect their interactions and dynamics.

The BCM mechanism (**Fig. 2A**) in our model encapsulates the effect of changes in the PF activity by either potentiating or depressing the synapse independently of CF input. This mechanism depends on 3 factors: the average of the recent activity of the PC, ρ_{PC}; the BCM threshold θ_M — which also depends on ρ_{PC}— and the instantaneous activity of the PF, ρ_{PF} (**Fig. 2B**). After an IO spike (**Fig. 2C**), a pause in SSpks leads to a CF pause, which causes a decrease in ρ_{PC}. The LTD component of plasticity due to the CSpk gives a negative change in synaptic weight also proportional to the ρ_{PF} (**Fig. 2D**). The plasticity threshold θ_M distinguishing depression from potentiation follows ρ_{PC}, that is θ_M lower than ρ_{PC} results in potentiation. Conversely, θ_M higher than ρ_{PC} leads to depression. Both these changes are proportional to activity ρ_{PF} for each synapse (see **Fig. 2E**). The total change in weight is the sum of the BCM and CSpk weights (**Fig. 2F**). The BCM plasticity mechanism has only one hard constraint limiting the potentiation of the PC to frequencies of 250 Hz, as firing rate beyond this rate is considered pathological.

Synaptic weights are stable across plasticity epochs

We hypothesized that synaptic weights would reach a new level of stability and stay at the level for subsequent plasticity events. To investigate these changes in synaptic weights across plasticity events we did the following simulations (see Methods), wherefor each epoch we gave the same frozen input as PF input. We started with the first epoch ("no plasticity") with the plasticity turned off and with static synaptic weights which were constant throughout this 120 s experiment. After this "no plasticity" epoch finished, BCM and LTD plasticity mechanisms were enabled and the same frozen input was replayed. At the end of this plasticity epoch, we took the last value of the filtered synaptic weights and turned it into the new static weights for the final epoch (after plasticity). Again the same input was given one

last time with the new static weights. This configuration enabled us to compare synaptic weights at the PF-PC synapse before and after plasticity. To evaluate the impact of plasticity on the weights, each experiment was performed 4 times with the same frozen input (**Fig. 2G-L**).

For both Upbound and Downbound zones the direction of change of the 500 synaptic weights for the 100 PC population (5 synapses per PC) was defined during the first "plasticity" epoch. The synaptic weights at this epoch were reduced in the Downbound zone and increased in the Upbound zone (**Fig. 2K-L**), suggesting that the intrinsic PC currents determined the plasticity direction. From the second epoch after plasticity we found that the weights were mostly stable, though a few changed in rank (**Fig. 2I-J**), indicating that the interaction between CSpk and PF inputs may drive these rank changes. In Downbound zones weights oscillated around the mean, indicating a faster rate of weight change, due to the higher intrinsic PC current (**Fig. 2K-L**). The Upbound zone, with a lower intrinsic drive, exhibited more synaptic weight stability after relaxation in epochs 3 and 4 (**Fig. 2G-H**).

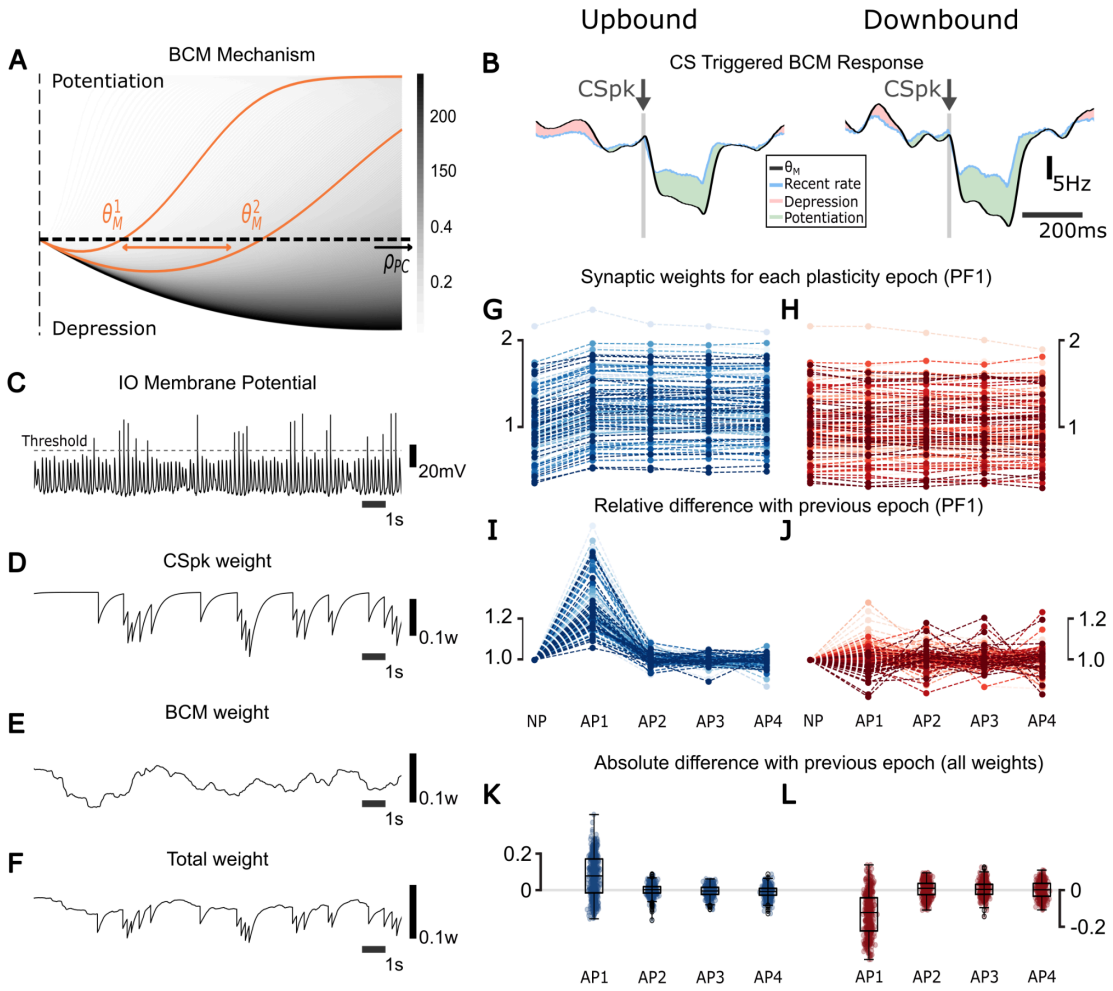

Figure 2 The plasticity direction differs between Upbound and Downbound micromodules. ***(A)*** *BCM mechanism: the positive side of the y-axis depicts potentiation and the negative depression. As the activity of the PC (x-axis) changes, the threshold (theta) follows. An increase in the activity leads to a higher theta which in turn increases the chances of depression (a larger part of the curve is negative). The same applies for a lower activity in PC, leading to higher chance of potentiation.* ***(B)*** *CSpk-triggered change in BCM. When there is a CSpk, the activity of the PC (blue) decreases. Theta (black) follows and goes lower than the PC activity, leading to potentiation (green). When theta is higher than the activity there is depression (red). This is shown for both Upbound and Downbound zones.* ***(C)*** *Trace of the IO membrane potential for Downbound coupled scenario.* ***(D)*** *The CSpk weight decreases proportionally to the instantaneous activity of the PF upon a CSpk.* ***(E)*** *The BCM potentiated response to the CSpk.firing frequency.* ***(F)*** *The total synaptic weight.* ***(G)*** *Synaptic weights of all PCs connecting to PF 1 before and after each plasticity (AP 1, 2, 3 and 4) experiment for the Upbound zones.* ***(H)*** *Same as G but for the Downbound zone.* ***(I)*** *Relative difference between the epochs (current weight divided by the one of the previous event) for Upbound zones.* ***(J)*** *Same as I but for the Downbound zones.* ***(K)*** *Boxplots depict absolute differences between the epochs for the whole population of weights (current weight minus previous weight) for Upbound zones.* ***(L)*** *Same as K but for the Downbound zones.*

Gap junction coupling creates a global phase and leads to synchronized firing

We hypothesize that gap junctions (i.e. "coupling") have an impact on IO STO synchrony in that strong coupling leads to higher synchrony. To quantify this effect, we looked at the STO oscillation phases over time. These were decomposed into a network level (global) phase and into an individual level (delta) phase to compare the difference between the individual and global phases (**Fig. S2-1A**). The global phase of STOs, representing average phase progression, was very stable in both coupled and uncoupled conditions (**Fig. S2-1B,S2-2B**). In the condition with coupled IO cells, oscillators phase-locked onto the global phase creating synchrony (**Fig. S2-1C**) not seen in the uncoupled case (**Fig. S2-2.C**), where oscillators behaved independently. To investigate whether the coupling also led to dynamically organized clusters in the IO, we calculated the pairwise Kuramoto phase (**Fig. S2-1D**). At the scale of one second (**Fig. S2-1E**), transient clustering could be observed, however clusters were not stable (**Fig. S2-1F-G**) and reflected random phase fluctuations driven by GABAergic CN input. At the scale of 30 s (quarter-time of the full simulation) no clear clustering was observed. Network synchrony peaked around IO spikes, but only for the coupled scenario (**Fig. S2-2A**).

Upbound PCs have a propensity for potentiation and Downbound PCs for depression

As it has been shown that PCs adaptively adjust their SSpk firing rate via CSpks to elicit blinks during eyeblink conditioning [74–76], we hypothesize that the direction of change of the PC firing rate depends on the intrinsic frequency of each PC microzone. Eyeblink conditioning is a classical associative learning paradigm where a neutral stimulus, such as light, is paired with an air puff that evokes reflexive eyelid closure so that the initially neutral stimulus can eventually trigger blinking. As argued previously [28], in this associative task, bidirectional changes in the SSpk activity are expressed in Upbound and Downbound zones during initial stages of training (**Fig. 3A**). Namely, the spontaneous activity of Downbound

PCs decreased during the initial stages of learning and the opposite happened for Upbound PCs. We looked at the results of the “no Plasticity” and “after Plasticity” epochs and found that our model reproduced these results, suggesting that the initial level of PC activity is enough for the BCM mechanism to establish the direction of plasticity (**Fig. 3B**). Notably, our model showed bidirectional changes at a longer timescale when compared to the experimental recordings (second and hundreds of milliseconds, respectively). PCs in our model were tuned to reproduce the experimental data (**Fig. 3C-D**), whereby Downbound PCs showed relatively high SSpks (~90 Hz) and CSpks (~1.3 Hz) firing frequencies, while Upbound PCs had lower average SSpk (~60 Hz) and CSpk [(~0.9 Hz), [9,28]]. Tuning PCs intrinsic currents resulted in the CF pause reproducing experimental observations (**Fig. 3E**).

The direction of plasticity was the same irrespectively of the absence or presence of IO gap junction coupling (**Fig. S3A-E**). For the Downbound micromodule, there was a small increase in the mean of the CSpk firing frequency in the uncoupled case with respect to the coupled case (**Fig. 3D** and **Fig. S3B**), which led to a wider distribution of the CSpk frequency squared coefficient of variation [(CV2);(**Fig. S3F**)].

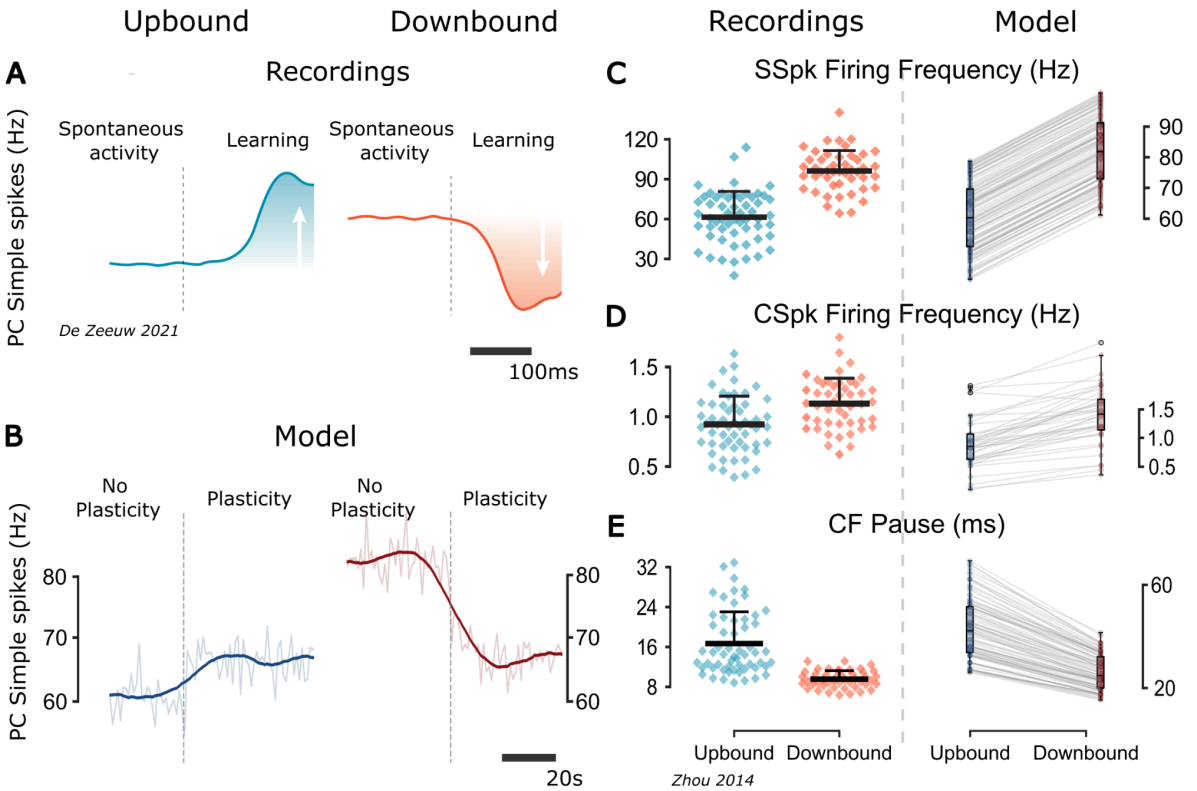

Figure 3. Comparison of experimental results and model results for Downbound and Upbound zones. ***(A)*** *Review from [28] showing the direction of plasticity of PC SSpk during learning for Upbound and Downbound zones.* ***(B)*** *Results from the model showing PC SSpk activity when plasticity mechanisms (BCM, LTD) are activated.* ***(C)*** *Comparison of experimental recordings adapted from [9] and model results of PC firing frequency, CSpk firing frequency (**D**) and CF pause duration (**E**). There is a significant difference in means across Upbound and Downbound modules for the SSpk (**t=-13.78, p<0.001; two-sample Student's t-test**), CSpk (**t=-4.59, p<0.001; two-sample Student's t-test**), and CF pause (**t=-12.52, p<0.001; two-sample Student's t-test**), which also has a smaller variance in the Downbound zone (**F=2.94, p<0.001; F-test using CCDF of F-distribution**).*

Inhibition followed by disinhibition of CN elicits CSpk

We hypothesized that specific characteristics of the input would elicit CSpks. We started by analysing the CSpk-triggered PSC (**Fig. 4A**) and we observed that the CSpks were promoted by specific oscillations present in the input. CSpks were evoked when the input carried specific phases and frequency (around 5-6 Hz), with a preference for reduced input just before the CSpk. At the level of the CN this translated to inhibition followed by disinhibition, which had previously been empirically observed by [77,78]. The decrease (following an increase) in PSC happened 60 ms before the bottom of the subthreshold oscillation (STO) of

the IO membrane response, which was closely related to the synaptic delay in the loop (10 ms between PC and CN and 60 ms between CN and IO). This suggests that CSpks had a preference for particular frequencies and phases of the input. A clear contrast is observed after plasticity, as in Upbound zones the sensitivity to the PSC oscillations was increased and reduced for Downbound zones.

The stimulation of the CN reseted the IO STOs (**Fig. 4B**), in line with experimental results [16]. We found that in the Upbound zone there was a lower CN spike frequency and lower amplitude of IO oscillations before the CN spike. Since there was more CN inhibition in the Downbound zone, we observed that lower CN spike frequency allowed for higher amplitude IO oscillation before the CN spike. In fact, we found that more CN inhibition slowed down the IO STOs, but also created more opportunity for IO spikes (**Fig. S4E**). In the Downbound zone, the CN spike did not have a significant effect on the IO oscillation after plasticity. This result suggests that the IO STOs are not completely driven by CN inhibition.

After the first "plasticity" epoch, the PC SSpk activity was increased for the Upbound zone and decreased for Downbound zone, resulting in both PC populations firing at about 60 Hz after plasticity (**Fig. 4C**). As a result, the CN activity was decreased for the Upbound and increased for the Downbound zone (**Fig. 4D**). Furthermore, the CSpk frequency was decreased for Upbound PCs and increased for Downbound PCs (**Fig. 4E**). The CV of the CF pause decreased for both Upbound and Downbound zones (**Fig. 4F**).

Investigating the effect of gap junction coupling, we observed that the uncoupled Downbound IO had on average a higher variance and higher CSpk firing frequency (**Fig. S4B**), leading to a higher variance of SSpk firing frequency for Downbound PCs (**Fig. S4A**). Nevertheless, the CN (**Fig. S4C**) and CF pause (**Fig. S4D**) were the same for both coupled and uncoupled conditions.

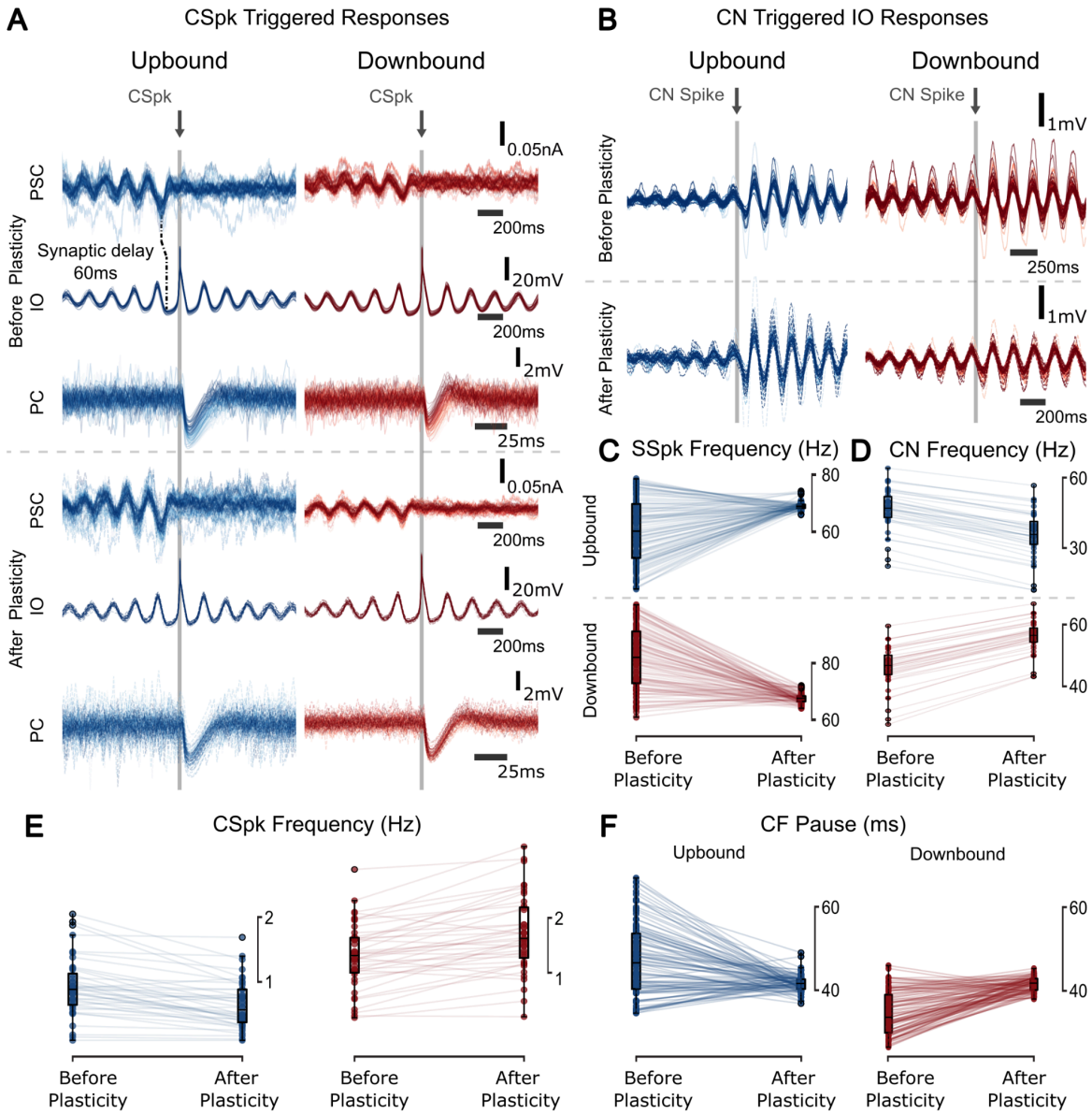

Figure 4. Spiking resonances after plasticity are zone dependent. (A) *CSpk triggered PSC (top), IO membrane potential (middle), and the PC membrane potential showing the CF pause (bottom). The synaptic delay between the PSC entering the PC, going through the CN (10 ms) and reaching the IO (50 ms). As the CN inhibition hits the bottom of the IO STO, a CSpk is elicited.* ***(B)*** *CN spike triggered membrane response of the IO, before and after plasticity.* ***(C)*** *Boxplots of SSpk frequency before and after plasticity. There there is a significant difference in the across the Upbound and Downbound zones before and after plasticity (before plasticity:* ***t=-13.90, p<0.001,*** *after plasticity:* ***t=-5.36, p<0.001; two-sample Student's t-test****) and the variance is also different after plasticity across the zones (****F=1.69, p=0.005; F-test using CCDF of F-distribution****). There is a significant difference across plasticity epochs for both zones (Upbound:* ***t=-7.64, p<0.001,*** *Downbound:* ***t=12.89, p<0.001; two-sample Student's t-test****). The variance of the SSpks after plasticity is also significantly different (Upbound:* ***F=59.88, p<0.001,*** *Downbound:* ***F=36.00, p<0.001; F-test using CCDF of F-distribution****).* ***(D)*** *Boxplots of CN spiking frequency before and after plasticity (before plasticity:* ***t=-3.26, p=0.002,*** *after plasticity:* ***t=9.15, p<0.001****, Upbound:* ***t=5.05, p<0.001,*** *Downbound:* ***t=-7.26, p<0.001****;* ***two-sample Student's t-test****).* ***(E)*** *CSpk frequency before and after plasticity (before plasticity:* ***t=3.98, p<0.001,*** *after plasticity:* ***t=9.44, p<0.001****,*

Upbound: ***t=2.99, p=0.004****, Downbound:* ***t=-2.81, p=0.006; two-sample Student's t-test****). The variance of CSpks is also different after plasticity across the zones (****F=2.91, p<0.001; F-test using CCDF of F-distribution****). (****F****) CF pause length is significantly different before plasticity (****t=-12.52, p<0.001; two-sample Student's t-test****). The length of the CF pause is significantly modulated by plasticity in both zones (Upbound:* ***t=6.37, p<0.001,*** *Downbound:* ***t=-13.00, p<0.001; two-sample Student's t-test****). The CF pause variance was smaller after plasticity (Upbound:* ***F=20.76, p<0.001,*** *Downbound:* ***F=9.34, p<0.001; F-test using CCDF of F-distribution****).*

Specific input frequency bands differentially drive plasticity

Our previous hypothesis was that specific characteristics of the input would affect CSpk generation. We expand this hypothesis to the whole loop and we hypothesise that different frequencies differentially influence the resonant dynamics of the olivocerebellar loop. Signals from different sensorimotor sources have different spectral properties, and PC population SSpks activity has been reported to contain bands from low delta [79] to high gamma [55] frequencies. To investigate how these different bands influence the loop dynamics under plasticity we inspected the filtered versions of the original PF signal. The filtered signals were normalized to keep the same spectral power (**Fig. 5A**), and were used in exact copies of the same network to compare the before and after plasticity activity of the cells across the different frequency bands (**Fig. 5B-D**). We found that CN dynamics were hardly modulated by the filter classes, indicating high level of signal divergence and mixing (**Fig. 5C**).

As judged both from SSpk (**Fig. 5B**) and CSpk (**Fig. 5D**) distributions, both Upbound and Downbound PC zones exhibited considerable frequency dependence, which varied qualitatively for the different bands, producing variation in the distribution of firing rates in the population. This was more often the case for SSPks in the Upbound zones than for Downbound zones.

While the direction of plasticity of CSpks activity qualitatively resembled physiological observations [9,28,54], frequency distributions were sensitive to plasticity under different bands, with lower input frequencies driving most of the variability. This was true for low frequencies (5-10 Hz band), where the CSpks activity was higher for Upbound

and Downbound zones. Furthermore, frequency bands larger than 10 Hz evoked similar SSpks and CSspks distributions after plasticity, indicating that the PC network response was robust to frequency variations.

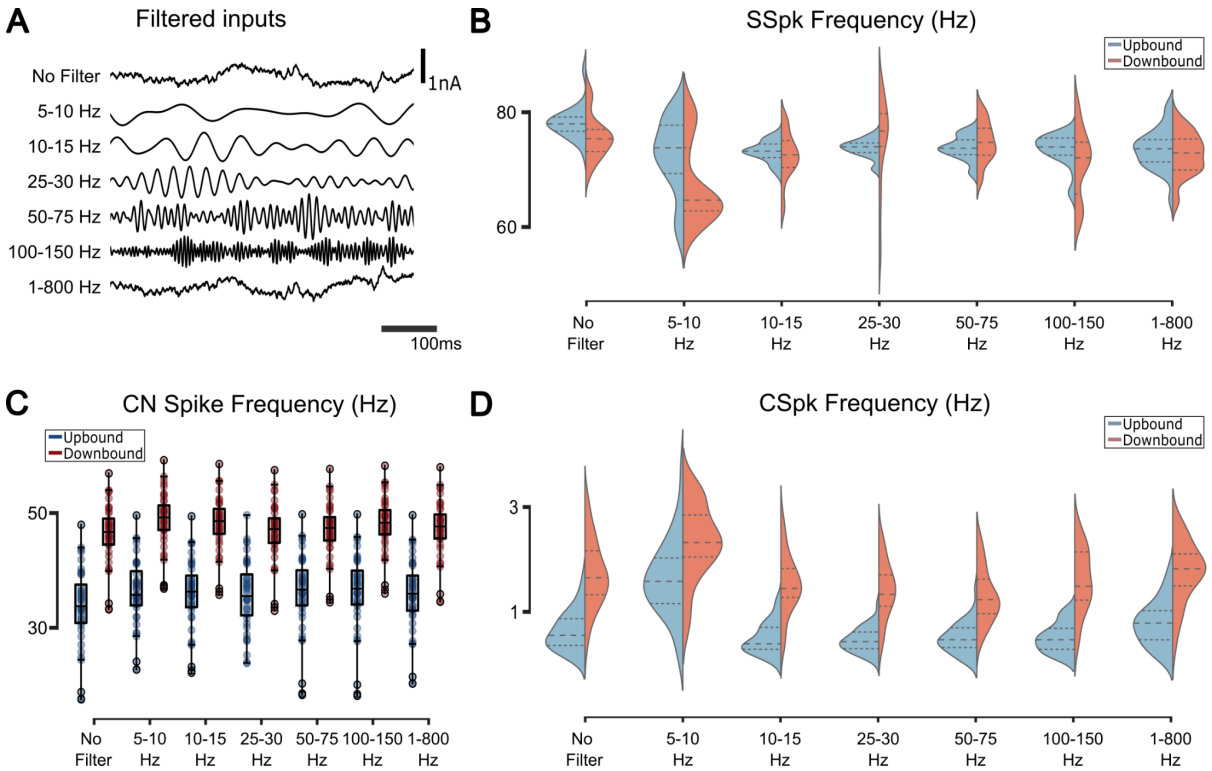

Figure 5. Response of the olivocerebellar model after plasticity for Upbound and Downbound zones for filtered inputs. ***(A)*** *Different types of filters used on the original input (no filter).* ***(B)*** *When comparing with the no filter input, the distribution of frequency of SSpks is always different across frequency bands for the Upbound zone and in the case of the Downbound it is different between the 25-30 and 50-75 Hz frequency bands (for statistics see* ***Table S1****). The distribution of the SSpk frequency is significantly different between Upbound and Downbound across the different filter inputs (see* ***Table S1*** *for statistics).* ***(C)*** *The CN spike frequency stays the same for all types of inputs across modules (see* ***Table S2*** *for statistics).* ***(D)*** *CSpks frequency stays the same for all types of inputs across modules (for statistics see* ***Table S2****). The response of the IO varies significantly for the 5-10 Hz frequency band (Upbound:* ***t=-7.86, p<0.001*** *and* ***D=0.75, p<0.001****, Downbound:* ***t=-4.04, p<0.001; two-sample Student's t-test*** *and* ***D=0.5, p<0.001; two-sample ks-test****).*

Differential CSpk response to PF input changes drives LTD in 5-10 Hz band

The largest differential plasticity responses were observed for the 5-10 Hz filtered input in the Downbound zone. Here we observed a large decrease in SSpk frequency after plasticity (**Fig. 5B**), with a twofold increase of CSpks (**Fig. 6A**). Before plasticity, the SSpk frequency was approximately the same for the 5-10 Hz filtered input and the "no filter" case, as the current

input power spectrum and weights were the same. We assumed that the decrease in SSpk frequency after plasticity originated from CSpk-triggered LTD. However, this assumption did not explain the increase in CSpk frequency for the 5-10 Hz filtered PF input.

We looked at the relationship between the STO frequency and CSpk frequency (**Fig. 6B**). We found that STO frequency and frequency-distribution width was lower in the Downbound than in the Upbound zone. For both Upbound and Downbound the STO frequency and IO spike frequency were inversely related. This was expected, as more CN inhibition slowed down the IO STOs (**Fig. S4E**), and created more opportunities for spikes. For both the Upbound and Downbound zone, 5-10 Hz input lowered the STO frequency further, while at the same time increased the IO spike frequency. The lowering of the STO frequency was more pronounced in the Upbound zone. We examined the IO spike-triggered PSC to understand further how the input characteristics affected CSpk occurrences (**Fig. 6C**). In general, for both IO unfiltered and 5-10 Hz input, IO spikes were preceded by oscillations below or at the lower range of the STO frequency (5.6 Hz for Upbound, 5.4 Hz for Downbound). For unfiltered noise, IO spikes were triggered by a small decrease in PSC amplitude, whereas for 5-10 Hz input, IO spikes were triggered by a shortening of the PSC oscillation period by 10 ms (**Fig. 6C**). Our results suggest that, for the unfiltered input (OU input), the smaller frequencies, which are similar to the STO frequency, have a bigger impact on the system.

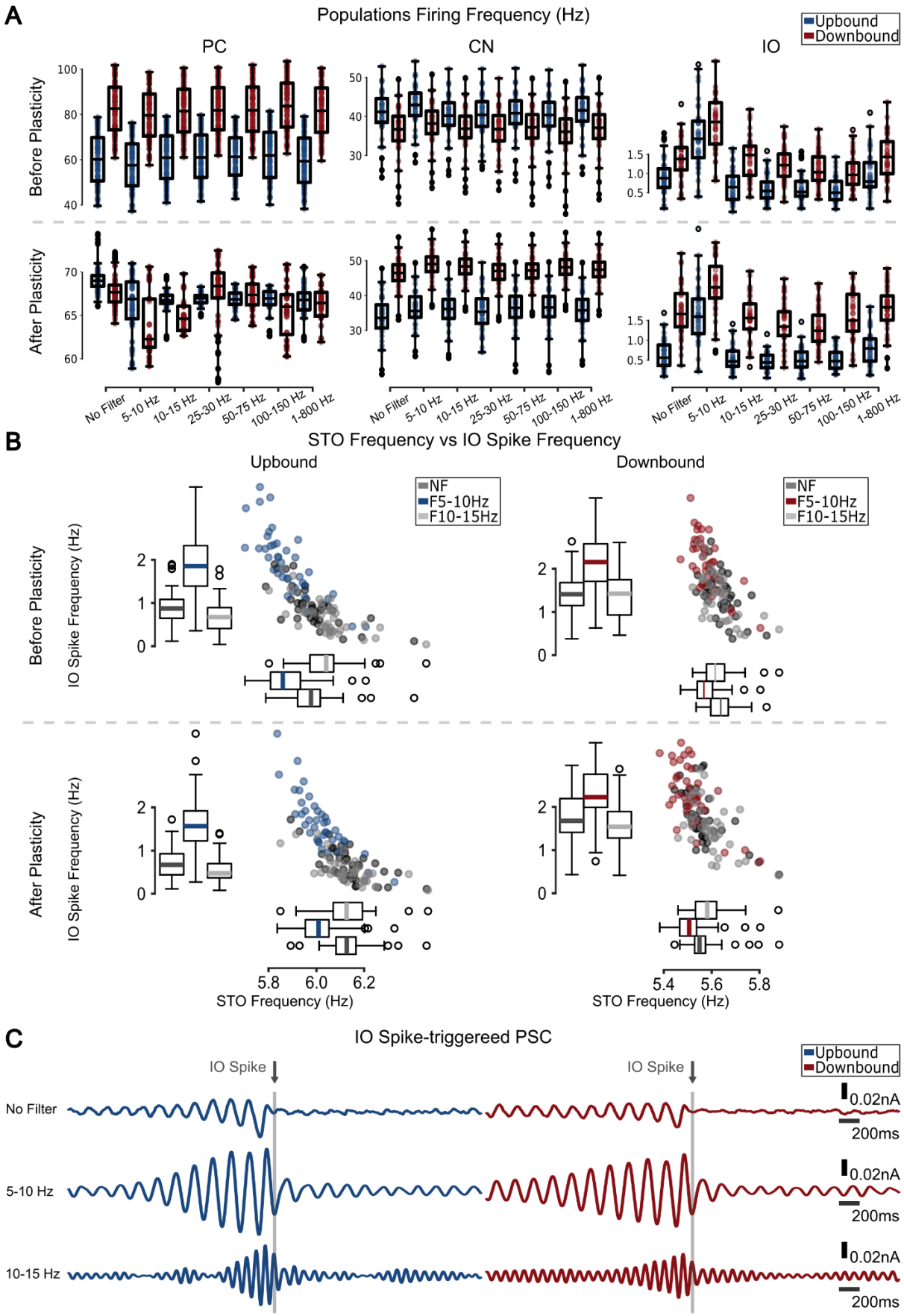

Figure 6. Input Filter 5-10Hz. (A) *Firing frequency distributions for each population before and after plasticity for different frequency bands.* ***(B)*** *STO frequency vs IO spike frequency*

for Upbound (left) and Downbound (right) zones for before (top) and after (bottom) plasticity. There seems to be an inverse relationship between STO frequency and IO spike frequency. To reduce the effect of the spike refractory period on STO frequency, it is here defined as the mean of the 25-75 percentile of the inverse of the phase period. For the 5-10 Hz filter in zebrin positive, STO frequency seems to decrease while STO spikes increase. For zebrin negative, STO frequency is lowered after plasticity, correlated to a higher baseline CSpk frequency and thus a less pronounced difference to the 5-10 Hz filter. ***(C)*** *IO spike triggered PSC for NF (top), 5-10 (middle) and 10-15 Hz (bottom) input filters. In general, IO spikes for The NF case seem to derive from entrainment followed by a final larger decrease in PSC. For 5-10 Hz filter, IO spikes seem to derive purely from entrainment to the oscillatory signal, with also a much clearer (larger amplitude) template before the spike.*

Gap junction coupling drives frequency selectivity

Following our previous hypothesis that gap junctions affect IO STO synchrony, we hypothesized that this change in STO synchrony will be reflected in the loop's response to different frequencies. We observed that the frequency selectivity of the IO was lost when the gap junction was uncoupled (**Fig. 7A**). The differences in the mean and distribution of CSpk and SSpk frequency after plasticity were much less pronounced within the zones in the uncoupled condition than in the coupled case. Furthermore, the higher IO spike frequency and lower STO frequency was completely lost for the Upbound zone, but was increased for the Downbound micromodule when the IO neurons were uncoupled (**Fig. 7B**). The loss of the inverse STO - IO spike frequency relationship in the Upbound zone co-occurred with a loss of the oscillatory response in the IO-spike triggered PSC (**Fig. 7C**). A higher CSpk frequency for the Downbound zone (**Fig. S3B**) led to a less pronounced loss of the inverse STO - IO spike frequency relationship. This suggests that the gap junction coupling has an effect upstream to the PC-CN and back to the IO as there is less variation in the CN inhibitory input onto the IO.

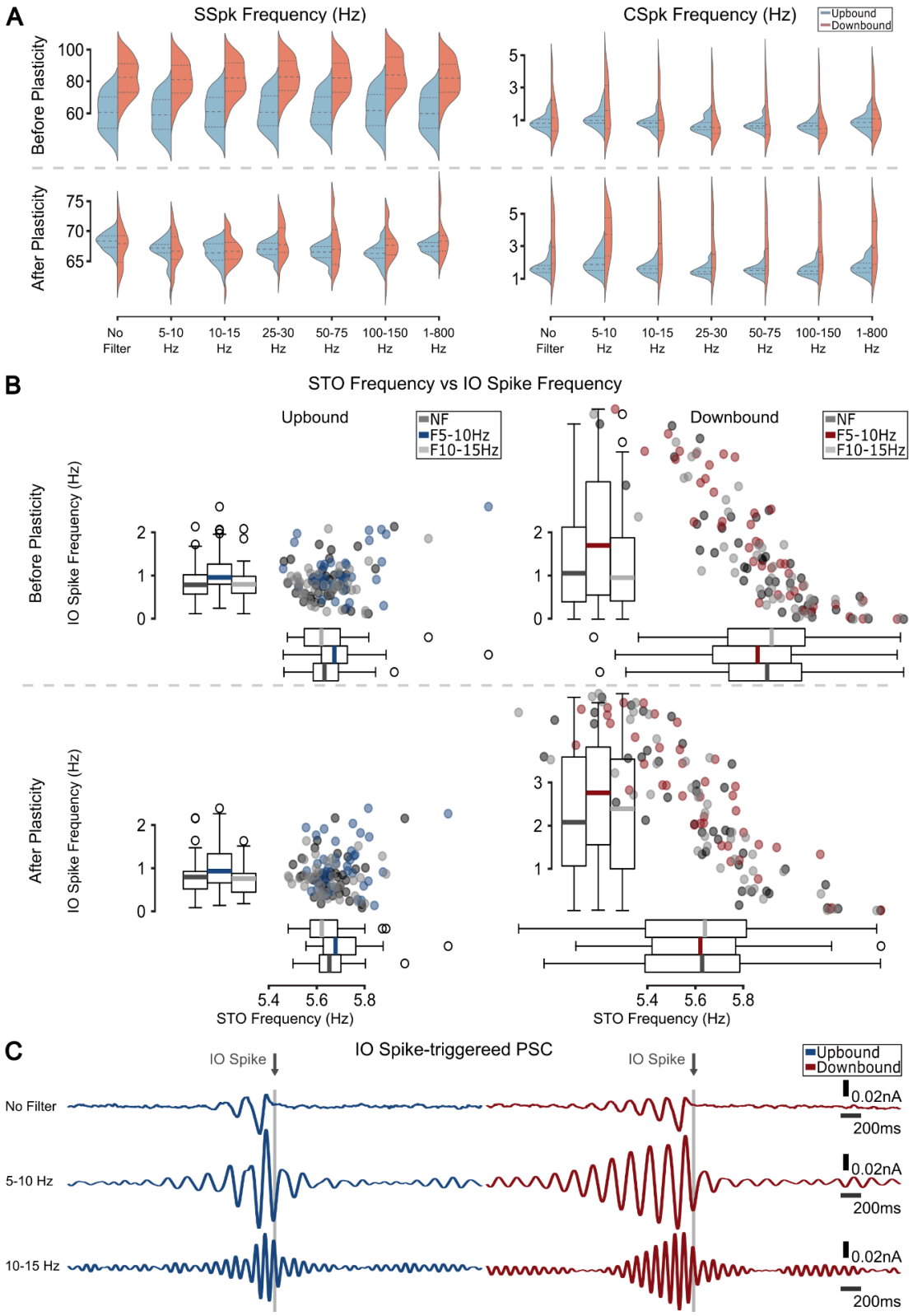

Figure 7. Gap junction drives frequency selectivity. (A) *Firing frequency distributions for SSpks (left) and CSpks (right) before and after plasticity for different frequency bands when gap junctions are deleted.* ***(B)*** *STO frequency vs IO spike frequency for Upbound (left) and Downbound (right) zones for before (top) and after (bottom) plasticity. Downbound IO has a wider range of STO frequency and as a result a wider range of IO spikes also.* ***(C)*** *IO spike triggered PSC response. Uncoupled Upbound zones lose or have much shorter entrainment phase, while the Uncoupled Downbound still shows strong oscillatory response.*

Discussion

How brains are able to maintain acquired sensorimotor patterns while plasticity is a function of reverberating activity in all elements of the system is a central problem in computational neuroscience. The olivocerebellar system is a particularly interesting case to study ongoing plasticity dynamics given that many of its neurons have a high level of intrinsic activity, organized in repeated feedforward loops. To examine the plasticity dynamics of the olivocerebellar system we developed a biologically meaningful model comprising both Upbound and Downbound micromodules. In designing our model, we applied a reverse engineering approach and remained agnostic with respect to the specific functions that the cerebellar modules compute, focusing on common closed loop dynamics of PF-PC plasticity subjected to resonances of IO spiking. We excluded input to the IO and CN from cortical and subcortical structures and treated IO activity exclusively as a function of CN feedback and intrinsic oscillatory activity. Using this network model formed by the most essential components we analysed resonant dynamics of the loop, PC-PF weight distributions and stability under different frequency inputs, as well as the influence of IO gap junctions on frequency responses across populations. After justifying our agnostic modeling approach, below we will discuss the main specific questions that were addressed by interrogating the model; these include (1), how steady state distributions of PC activity capture directions of plasticity in Upbound and Downbound modules, (2) which PF input frequencies most likely evoke CSpks, (3) how the synaptic weights of the PFs of both modules stabilize, and (4) to what extent this stabilization depends on gap junction coupling in the IO.

Agnostic vs ANN models of the cerebellum

Existing modeling approaches for this system equate the cerebellar network with strong and close analogies to artificial neural networks (ANNs) and models rooted in the

Marr-Albus-Ito hypothesis regarding cerebellar function [80,81]. While top-down ANN models hold explanatory power, they can have certain shortcomings. Top-down approaches depart from assumptions about how and what the cerebellum learns; they usually comprise forward models, adaptive filters and/or hierarchical control components. In all these approaches the CSpk plays the essential role of supervised/reward-based learning feedback [82–87]. ANNs do not focus on the consequences of biological complexity that are outside of the realm of the assumed output, and thus cannot be used to ask, in a hypothesis-free manner, about the consequences of anatomy (circuit topography), physiology (multi-site plasticity) and dynamics, which are not strictly necessary to explain pattern recognition [10,88–90]. We therefore argue that we can calculate the implications of certain biological structures most reliably if our computational models represent them faithfully, while remaining as agnostic as possible about the potential functions and mechanisms involved.

Steady state distributions of PC activity

The isolated olivocerebellar loop model was used to inspect PF-PC weight distributions and their stability after repeated presentations of stochastic input ("Frozen Noise"). In this model, PF-PC synapses are subject to two types of plasticity, BCM and CSpk LTD. The BCM rule is a Hebbian activity dependent learning rule, and as such is expected to reflect statistical regularities in the input [91,92]. However, in a biophysically plausible setting with a large set of parameters and feedback there is no guarantee that IO and PC responses remain bounded over time. To examine weight convergence, we verified the weight values after multiple epochs of 'frozen noise'. We found that synaptic weight distributions and firing rates stabilized across epochs for both Upbound and Downbound micromodules. After an initial transient, Upbound zones displayed more weight stability across epochs, while Downbound modules had weights that oscillated, and thus were more sensitive to loop dynamics. In effect, plasticity tuned PC activities in the same direction as observed in

physiological experiments [9,28,54] (**Fig. 3**). Our model showed how module specific intrinsic PC firing rates acted on the PC synaptic weights and gave rise to the direction of plasticity. Effectively, we can conclude that interaction between intrinsic PC firing rates and the recent PC rate jointly established a preferred activity level for each PC population, which was reached after plasticity is activated for a few hundred seconds. The intrinsic current established a rate preference that acted as a corrective "elastic force" on the weights. In the case of the Downbound module this correction appeared underdamped, whereas it was overdamped in the Upbound zone. This leads us to predict a higher changeability of synaptic weights in Downbound zones, as the PC intrinsic rate is kept farther from circuit equilibrium in the case of Downbound zones. This is well in line with the protein expression levels of PCs; most of the proteins that are known to be implicated in synaptic plasticity are more prominently expressed in the Downbound zones than those of the Upbound zones [28,54,93]. In this respect it is important to note that recent transcriptomics studies indicate that the subdiversity of different PC microzones is even greater than the two main categories of Upbound and Downbound modules, particularly in higher species [53,94,95]. Hence, future models will need to consider whether to incorporate their properties to fully capture the heterogeneity of all PC populations.

Thus, while zone-specific PC characteristics are known to be intrinsic [9,28,53,54], our model reveals that the olivocerebellar loop mechanisms enhance this functional difference and drive it to stability, engaging interactions of BCM and CSpk-dependent long-term plasticity rules.

Input Frequency Dependent Responses

Changes of weight of specific PCs were strongly determined by their recent input, both in terms of PF and CF input. Recent firing rate acted as a low pass proxy to history of inputs, while the CSpk timing was strongly determined by the phase state of the IO. We

observed a strong preference for specific frequencies and phases of the stochastic PF input and showed that CSpks probabilities were modulated by specific temporal features of this input (**Fig. 4A-B**). As the state of the IO was subject to CN population drive, we showed that the plasticity of the overall system was frequency-dependent.

Our choice of using OU noise [66] was motivated by emulating arbitrary input that may exhibit any frequency and any phase combination. In the long interval of our plasticity epochs (120 s), this OU input contained very different frequency compositions. It was therefore expected that the influence of the specific frequencies contained in the different input PF bundles would differentially drive the production of IO's feedback, both in phase and in spiking. The variability of the IO feedback and the resulting jitter in the latency of the CSpk response across trials has also been observed experimentally [7,96] and can be explained by phase shifts of IO STOs [35]. We analyzed the extent of the input frequency dependence by filtering frozen noise inputs to include specific frequency bands. Plasticity was subjected to these frequencies, which led it to respond differently to signals with different frequency composition. There were very significant differences in SSpk distributions to filtered inputs, which was particularly apparent in Downbound zones. Specifically, we found that our modelled system responded preferentially to the 5-10 Hz frequency band, which overlapped with the IO STO frequency (5-6 Hz), indicating that specific ranges of PF frequency bands led this model closer to physiological responses.

When we further investigated the relation between STO frequency and IO spike frequency, we found that they were inversely related for both Upbound and Downbound modules. This was due to higher CN inhibition in the Upbound zone, which, by slowing down IO STOs, created more opportunity for IO spikes. In the Downbound zone the CN inhibition was lower, which created less opportunity for the IO spikes, due to slower STOs.

Stability of synaptic weights of PFs

The overarching question that motivates our model is the apparent dilemma between stability of acquired sensorimotor patterns and ever changing synaptic strengths. However, we did not specifically test the loop in a behaviorally-relevant setting, rather we examined the general case of any arbitrary input. Future research with our model could study input signals that more closely represent the contingencies of sensorimotor behavior, with their specific frequencies and phases, related to the interaction to the body and other brain regions. Upcoming effort could focus on adding the excitatory input to the IO from the MDJ [16] and even the CN [13]; oscillatory gating of the granular layer via Golgi cells [10,97]; and/or inhibition from the MLIs [98,99]. Out of these missing excitatory inputs, the absence of the excitatory loop via the MDJ is a notable exclusion from our current model, as the CN is believed to effectively produce excitatory potentials onto the IO via the MDJ. The counterintuitive but significant phenomenon from the excitatory branch of the loop is that excitation arrives considerably earlier than inhibition in the olive and produces earlier CSpks. The inhibition from the CN to the IO has a very long latency, of over 50ms [34,100,101]. The question arises as to why inhibition would be so delayed with respect to the excitation. It is known that electrical stimulation of the CN produces early CSpks (4-8 ms) through the excitatory pathway via the MDJ, which we excluded in this research [15]. We predict that interactions between early and late CSPks will be a part of our understanding of how the olivocerebellar system participates in the acquisition and maintenance of sensorimotor sequences, in the context of ongoing processing of cortico-thalamic, basal ganglia signals and ascending sensory signals, a foremost problem for upcoming bottom-up computational models of the cerebellum [102].

Impact of gap junction coupling on stabilization

Gap junctions can cause synchronized IO spikes, in both Upbound and Downbound zones, leading to a global phase in which many individual IO neurons are coupled [16,103]. When the gap junctions were abolished, the variability of the IO spike rates in the IO population was almost absent. Notably, the IO cells could momentarily decouple to advance or delay an oscillatory cycle. This result suggested that the gap junctions have a critical influence on the frequency selectivity of the system. Indeed, when tested, we found that the frequency selectivity due to the difference in strength of the CN input, highlighted above, was lost in the absence of IO gap junction coupling. As CN inhibition turned out to not completely shape the IO STOs, this could indicate that the interplay between CN inhibition and IO gap junction coupling is at the core of this STO - IO frequency relationship. It should be noted that the interaction between GABAergic CN input to the IO and regulation of the coupling strength as well as the relevance of coupling in the IO for the prominence of its STO's has been the subject of many experimental studies. Both relations have been confirmed at the morphological, electrophysiological and pharmaceutical level, *in vivo* as well as *in vitro* [15,16,29,30,32–37,41,79,104]. The relationship between the level of STO's and IO frequency band is underscored by the finding that Upbound and Downbound modules showed different correlation strengths in this respect. Thus, as the level of gap junction coupling facilitates IO resonance and as there are module-specific interactions, our data imply that the temporal pattern selectivity processing across Upbound and Downbound micromodules is enhanced by dynamic regulation of electrotonic coupling in the IO.

Methods

Parallel fiber bundles

We simulate the PF input, representing the activity of PF bundles, as an Ornstein-Uhlenbeck (OU) process:

$$\frac{dI^{(PF)}{}_{OU}}{dt} = \frac{I^{(PF)}{}_{OU_0} - I^{(PF)}{}_{OU}}{\tau^{(PF)}{}_{OU}} + \frac{\sigma^{(PF)}{}_{OU}}{\sqrt{\tau^{(PF)}{}_{OU}}}\xi \qquad \text{Eq. (1)}$$

where ξ is a Gaussian random variable with mean $\mu = 0$ and standard deviation $\sigma = 1$ that scales with units of $s^{-0.5}$. The mean is $I^{(PF)}{}_{OU_0}$ and the variance —the integral of the power spectral density— is equal to σ^2. The noise intensity is defined as $\sigma^2\tau$. Parameter values in the model are shown in **Table 1**.

Table 1. Parameters of the Ornstein-Uhlenbeck processes

Parameters	Baseline current I_{OU_0} (nA)	OU time constant τ_{OU} (ms)	OU standard deviation σ_{OU}
PF	1.3	50	0.25
IO	-0.3	50	0.3

PC and CN neuronal models

The PC and CN populations are modeled as adaptive exponential integrate-and-fire (AdEX) models [105]. The general cell equations for the PC and CN are described as:

$$\frac{dV}{dt} = \frac{1}{C_m}\left(-g_l\left(V - V_l\right) + g_l\Delta_T e^{\left(\frac{V-V_T}{\Delta T}\right)} + \sum_i I^{(i)} - w\right) \qquad \text{Eq. (2)}$$

$$\frac{dw}{dt} = \frac{a\left(V-V_l\right)-w}{\tau_w} \qquad \text{Eq. (3)}$$

Here, Eq. 2 describes the membrane potential dynamics, while Eq. 3 shows the dynamics of the adaptation value. The $\sum_i I^{(i)}$ refers to the sum of the currents specific to the PC and the CN (where $i = PC, CN$); Δ_T is the slope factor; V_T is the threshold potential; w is the adaptation variable; a is the adaptation coupling factor, and τ_w is the adaptation time constant. The slope factor Δ_T is a quantification of the sharpness of the spike, which can be seen as the sharpness of the sodium activation curve if the activation time constant is ignored [106]. The parameters of all AdEx cells, both CN and PC, are randomized (see **Table 2**). Parameters are sampled without replacement from a corresponding population-sized list, spanning the listed range in the table. Hence, each cell in the population will display individual differences in firing properties. When a spike happens both the membrane potential and the adaptive variables are updated. The actual threshold potential $V_{cut} = V_T + 5\Delta_T$ is used for the neuron models. When the potential reaches V_{cut} (see **Table 2**), a spike occurs and both the membrane potential V is reset to V_r, and the adaptation variable w is updated to the reset adaptation current b and then decays until either reaching 0 or the next spike time [107].

$$@Cell\ spike\text{:}\ V = V_r;\ w \mathrel{+}= b \qquad \text{Eq. (4)}$$

Our goal for using the randomization of parameters is to have variability across the cells in each population. Since the CN is inhibited by the PC we will already have enough variability in the inhibitory current as each PC is different. Also, the CN cells have their own variability across the parameters. Hence, we do not randomize the intrinsic current I_{int} of the CN as we can then see the direct effect of one PC onto the CN.

Table 2. Parameters of the AdEx cell types

Parameters	PC	CN
Membrane capacitance C_m (pF)	$75 \pm 1.0[N_{PC}]$	$281 \pm 1.0[N_{CN}]$
Leakage conductance g_l (nS)	$30 \pm 1.0[N_{PC}]$	$30 \pm 1.0[N_{CN}]$
Leakage reversal potential V_l (mV)	$-70.6 \pm 0.5[N_{PC}]$	$-70.6 \pm 0.5[N_{CN}]$
Threshold potential V_T (mV)	$-50.4 \pm 0.5[N_{PC}]$	$-50.4 \pm 0.5[N_{CN}]$
Slope factor Δ_T (mV)	$2 \pm 0.5[N_{PC}]$	$2 \pm 0.5[N_{CN}]$
Adaptation time constant τ_w (ms)	$144 \pm 2.0[N_{PC}]$	$30 \pm 1.0[N_{CN}]$
Adaptation coupling factor a (nS)	$4 \pm 0.5[N_{PC}]$	$4 \pm 0.5[N_{CN}]$
Reset potential V_r (mV)	$-70.6 \pm 0.5[N_{PC}]$	$-65 \pm 0.5[N_{CN}]$
Reset adaptation current b (nA)	$0.0805 \pm 0.001[N_{PC}]$	$0.0805 \pm 0.001[N_{CN}]$
Intrinsic current I_{int} (nA)	$0.35 \pm 0.21[N_{PC}]$	1.2

Purkinje cell Currents

For the PC, there are 2 currents denoted $I^{(PC)}{}_{int}$ and I_{PF}. The former is the activation (intrinsic) input current given to the cell to tune the desired intrinsic firing frequency distribution. The latter is the postsynaptic current (PSC) input entering the PC soma from the PFs (**Fig. 1A**).

$$\sum I_{PC} = I_{PF} + I^{(PC)}{}_{int} \qquad \text{Eq. (5)}$$

Cerebellar nuclei Synaptic Currents

The CN currents are shown in Eq 5, where $I^{(CN)}{}_{int}$ is the intrinsic firing of the CN and $I^{(CN)}{}_{PC}$ is the inhibitory projection from the PC. When the PC is not spiking, $I^{(CN)}{}_{PC} = 0nA$,

however, upon a PC spike, $I^{(CN)}{}_{PC}$ is updated by $\gamma^{(CN)}{}_{PC}$(see **Table 6**). This means that the total current $I_{int} - I^{(CN)}{}_{PC}$ will be smaller and the CN will spike less (inhibition from PC).

$$\sum I_{CN} = I^{(CN)}{}_{int} - I^{(CN)}{}_{PC} \qquad \text{Eq. (6)}$$

Inferior olive model

The IO model is based on the De Gruijl model [108] —a modification of the Schweighofer model [109] with an added axonic current. The general cell equations for the model are shown below:

$$C_m \frac{dV_s}{dt} = -\sum I^{(s)} + I^{(s)}{}_{app} + I^{(IO)}{}_{OU} + I^{(IO)}{}_{CN} \qquad \text{Eq. (7)}$$

$$C_m \frac{dV_d}{dt} = -\sum I^{(d)} + I^{(d)}{}_{app} \qquad \text{Eq. (8)}$$

$$C_m \frac{dV_a}{dt} = -\sum I^{(a)} \qquad \text{Eq. (9)}$$

$$\frac{dI^{(IO)}{}_{OU}}{dt} = \frac{I^{(IO)}{}_{OU_0} - I^{(IO)}{}_{OU}}{\tau^{(IO)}{}_{OU}} + \frac{\sigma^{(IO)}{}_{OU}\xi}{\sqrt{\tau^{(IO)}{}_{OU}}} \qquad \text{Eq. (10)}$$

Where, the membrane potential specific to each compartment, somatic s, dendritic d and axonic a is represented with V_i (where $i = s, d, a$). The equations for the ionic conductances of the general cell are shown in **Table 3** and their parameters in **Table 4**. All parameters are randomized in the same way as for the AdEx parameters. The IO receives an a noise input $I_{IO_{OU}}$ modeled as an OU process (similarly to the PF input, see **Table 1**). With this input we model the baseline firing rate of the IO as well as modeling inputs from other brain regions. Furthermore, the input from the CN onto the IO is modeled by the differential equation $I_{IO_{CN}}$.

Finally, two applied currents $I^{(i)}_{app}$ (where $i = s, d$) are in the dendrites and somatic compartments. These are used when adding external current into the cell. For instance, $I^{(s)}_{app}$ is used when receiving a copy of the US of the eyeblink experiment. The dynamics of each activation or inactivation variable (see **Table 5**) is given by the differential equation below. In this equation z indicates the variables $h, k, l, n, x, q, r, s, h_a$ and x_a. There are 2 exceptions, m and m_a which have a small enough τ that they are approximately equal to their steady-states (m_∞ and m_{∞_a}, respectively).

$$\frac{dz}{dt} = \frac{(z_\infty - z)}{\tau_z} \qquad \text{Eq. (11)}$$

Table 3. Ionic conductances of the IO cell

Somatic currents $\sum I_s$	Dendritic currents $\sum I_d$	Axonic currents $\sum I_a$
$I^{(s)}_{Na} = g_{Na} m_\infty^3 h(V_s - V_{Na})$	$I^{(d)}_{Ca_h} = g_{Ca_h} r^2 (V_d - V_{Ca})$	$I^{(a)}_{Na} = g_{Na_a} m_{\infty_a}^3 h_a (V_a - V_{Na})$
$I^{(s)}_{Ca_l} = g_{Ca_l} k^3 l (V_s - V_{Ca})$	$I^{(d)}_{K_{Ca}} = g_{K_{Ca}} s (V_d - V_K)$	$I^{(a)}_{K_a} = g_{K_a} x_a^4 (V_a - V_K)$
$I^{(s)}_{K_{dr}} = g_{K_{dr}} n^4 (V_s - V_K)$	$I^{(d)}_c = g_c (V_d - V_{de}) f(V_d - V_{de})$	$I^{(a)}_{la} = g_{la} (V_a - V_l)$
$I^{(s)}_{K_s} = g_{K_s} x_s^4 (V_s - V_K)$	$I^{(d)}_{ld} = g_{ld} (V_d - V_l)$	$I^{(a)}_{sa} = \frac{g_{int}}{p_2} (V_a - V_s)$
$I^{(s)}_h = g_h q (V_s - V_h)$	$I^{(d)}_{sd} = \frac{g_{int}}{(1-p)} (V_d - V_s)$	
$I^{(s)}_{ls} = g_{ls} (V_s - V_l)$		
$I^{(s)}_{ds} = \frac{g_{int}}{p} (V_s - V_d)$		
$I^{(s)}_{as} = \frac{g_{int}}{(1-p_2)} (V_s - V_a)$		

Table 4. Parameters of the IO Standard Cell

Conductances (mS/cm^2)		Reversal Potentials (mV)	
g_{Na}	$150 \pm 1.0[N_{IO}]$	V_{Na}	$55 \pm 1.0[N_{IO}]$
g_{Ca_l}	$1.4 \pm 0.05[N_{IO}]$	V_{Ca}	$120 \pm 1.0[N_{IO}]$
$g_{K_{dr}}$	$9.0 \pm 0.1[N_{IO}]$	V_K	$-75 \pm 1.0[N_{IO}]$
g_{K_s}	$5.0 \pm 0.1[N_{IO}]$	V_h	$-43 \pm 1.0[N_{IO}]$
g_h	$0.12 \pm 0.01[N_{IO}]$	V_l	$10 \pm 1.0[N_{IO}]$
g_{ls}	$0.017 \pm 0.001[N_{IO}]$	Membrane Capacitance (μF/cm^2)	
g_{Ca_h}	$4.5 \pm 0.1[N_{IO}]$	C_m	$1.0 \pm 0.1[N_{IO}]^2$
$g_{K_{Ca}}$	$35 \pm 0.5[N_{IO}]$	Cell Morphology	
g_{ld}	$0.016 \pm 0.001[N_{IO}]$	g_{int}	$0.13 \pm 0.001[N_{IO}]$
g_{Na_a}	$240 \pm 1.0[N_{IO}]$	p	$0.25 \pm 0.01[N_{IO}]$
g_{K_a}	$240 \pm 0.5[N_{IO}]$	p_2	$0.15 \pm 0.01[N_{IO}]$
g_{la}	$0.017 \pm 0.001[N_{IO}]$		

Table 5. Steady-state activation/inactivation and time constants of IO ionic conductances

I	Steady-state Activation/Inactivation	Time constant τ (ms)	Forward rate function α	Backward rate function β
I_{Na}	$m_\infty = \frac{1}{1+e^{-\left(\frac{30+V_s}{5.5}\right)}}$			
	$h_\infty = \frac{1}{1+e^{\frac{70+V_s}{5.8}}}$	$\tau_h = 3e^{-\left(\frac{40+V_s}{33}\right)}$		
I_{Ca_l}	$k_\infty = \frac{1}{1+e^{-\left(\frac{61+V_s}{4.2}\right)}}$	$\tau_k = 5$		
	$l_\infty = \frac{1}{1+e^{\frac{85.5+V_s}{8.5}}}$	$\tau_l = 35 + \frac{20e^{\left(\frac{160+V_s}{30}\right)}}{1+e^{\left(\frac{84+V_s}{7.3}\right)}}$		
$I_{K_{dr}}$	$n_\infty = \frac{1}{1+e^{-\left(\frac{3+V_s}{10}\right)}}$	$\tau_n = 5 + 47e^{\left(\frac{50+V_s}{900}\right)}$		
I_{K_s}	$x_{\infty_s} = \frac{\alpha_{x_s}}{\alpha_{x_s}+\beta_{x_s}}$	$\tau_{x_s} = \frac{1}{\alpha_{x_s}+\beta_{x_s}}$	$\alpha_{x_s} = \frac{0.13(V_s+25)}{1-e^{-\left(\frac{25+V_s}{10}\right)}}$	$\beta_{x_s} = 1.69e^{-0.0125(35+V_s)}$
I_h	$q_\infty = \frac{1}{1+e^{\frac{80+V_s}{4}}}$	$\tau_q = \frac{1}{e^{-(14.6+0.086V_s)}+e^{-(1.87+0.07V_s)}}$		
I_{Ca_h}	$r_\infty = \frac{\alpha_r}{\alpha_r+\beta_r}$	$\tau_r = \frac{5}{\alpha_r+\beta_r}$	$\alpha_r = \frac{1.7}{1+e^{-\left(\frac{5+V_d}{13.9}\right)}}$	$\beta_r = \frac{0.02(V_d+8.5)}{e^{\left(\frac{8.5+V_d}{5}\right)}-1}$
$I_{K_{Ca}}$	$s_\infty = \frac{\alpha_s}{\alpha_s+\beta_s}$	$\tau_s = \frac{1}{\alpha_s+\beta_s}$	$\alpha_s = min([Ca^{2+}]_0, 0.01)$ $[Ca^{2+}]_0 = 2 \cdot 10^{-5}[Ca^{2+}]$	$\beta_s = 0.015$
I_{Na_a}	$m_{\infty_a} = \frac{1}{1+e^{-\left(\frac{30+V_a}{5.5}\right)}}$			
	$h_{\infty_a} = \frac{1}{1+e^{-\left(\frac{60+V_a}{5.8}\right)}}$	$\tau_{h_a} = 1.5e^{-\left(\frac{40+V_a}{33}\right)}$		
I_{K_a}	$x_{\infty_a} = \frac{\alpha_{x_a}}{\alpha_{x_a}+\beta_{x_a}}$	$\tau_{x_a} = \frac{1}{\alpha_{x_a}+\beta_{x_a}}$	$\alpha_{x_a} = \frac{0.13(V_a+25)}{1-e^{-\left(\frac{25+V_a}{10}\right)}}$	$\beta_{x_a} = 1.69e^{-0.0125(35+V_a)}$

Three morphological parameters determine the electrotonic properties of the three-compartmental model: the ratio of the somatic area to the total somatic and dendritic

surface area p; the ratio of the somatic area to the total somatic and axonic surface area p_2, and the electrotonic coupling conductance between the 3 compartments. The current flowing from the somatic into the dendritic compartment I_{sd} and from the dendritic into the somatic compartments I_{ds}, as well as the leakage currents for the soma I_{ls} and for the dendrites I_{ld} are represented in this model [109]. We also have the current flowing out from the soma into the axon I_{sa} and from the axon into the soma I_{as} as well as the leakage for the axonic compartment I_{la} [108]. Furthermore, the dynamics of the calcium concentration $\left[Ca^{2+}\right]$ is defined as follows:

$$\frac{d\left[Ca^{2+}\right]}{dt} = -\ 3.0 I_{Ca_h} - 0.075\left[Ca^{2+}\right] \qquad \text{Eq. (12)}$$

Two distinct types of calcium currents exist in the IO neuron: a low-threshold current I_{Ca_l} located in the soma and a high-threshold current I_{Ca_h} located in the dendrites [32,110]. As the window of conductance of I_{Ca_l} is around the resting membrane potential, the IO cell is excited in response to hyperpolarizing currents [32,110]. On the other hand, I_{Ca_h} is non-inactivating. Thus, a depolarizing dendritic input results in a prolonged plateau potential. As calcium enters the dendrites, the calcium-activated potassium current $I_{K_{Ca}}$ is activated. This current abruptly terminates the plateau potential after about 30 milliseconds [32,110]. Due to the long time constant (several hundred milliseconds) of $I_{K_{Ca}}$, there is a long afterhyperpolarization which, in turn, de-inactivates I_{Ca_l} resulting in a postinhibitory rebound spike. This current contributes to the subthreshold oscillations as it contributes to amplitude and frequency [109,111]. Furthermore, somatic sodium spikes are generated with the sodium current I_{Na}. These are terminated by an outward delayed rectifier potassium current $I_{K_{dr}}$

[32,110]. Finally, the axon hillock includes a sodium current I_{Na_a} (whose inactivation function was altered to allow for the generation of bursts of spikes) and potassium current I_{K_a} [108].

Synapses

Table 6 shows the parameters and synaptic delays for each synapse in the model. The synaptic delay and time constants were chosen from literature for the PC to CN and the CN to IO delays [101,108,112–115]. The rest of the values were chosen to reproduce electrophysiological results as shown in **Fig. 3**.

Table 6. Values for synapses

Synapses	Parameters	Values
PF-PC	Moving threshold θ_{M_0}	60 Hz
	Threshold time constant τ_M	15 ms
	CSpk induced LTD constant A_{CSpk}	-0.01 nA
	CSpk induced LTD time constant τ_{CSpk}	350 ms
PC-CN	Inhibitory current from PC to CN $\gamma^{(CN)}_{PC}$	0.004 nA
	Synaptic delay	10 ms
CN-IO	Inhibitory current from CN to IO $\gamma^{(IO)}_{CN}$	-1.8 nA
	IO_{CN} time constant $\tau^{(IO)}_{CN}$	30 ms
	Synaptic delay	50 ms
IO-IO	Coupling conductance g_c	0.00125 mS/cm^2
IO-PC	Inhibitory current from IO to PC $\gamma^{(PC)}_{IO}$	0. 22 nA
	$I^{(PC)}_{IO}$ time constant $\tau^{(PC)}_{IO}$	30 ms
	Synaptic delay	15 ms

PF-PC connectivity

Each PC receives input from 5 PF bundles with different (meta)synaptic weights. These weights are sampled from a uniform distribution and normalized to a sum of 5. This resembles a draw from a scaled symmetric Dirichlet distribution with concentration parameter alpha>1, i.e. the values are favored to the center of the simplex. The PSC I_{PF} (see PC model) is calculated as:

$$I_{PF} = \frac{1}{5}\sum_{j}^{N_{PF}} I_j w_j \qquad \text{Eq. (13)}$$

PF-PC Plasticity

The plasticity mechanism between the PF bundles and PCs consists of an intrinsic homeostatic mechanism w_{BCM} and a long-term depression (LTD) mechanism w_{CSpk}. The homeostatic mechanism is based on the Bienenstock, Cooper, and Munro (BCM) plasticity mechanism [116]. LTD happens at the IO spike. The final weight is as shown in Eq 13. Where, i is the PC (where $i = 1,\ldots,100$) and j is the synapse of that PC (where $j = 1,\ldots,5$).

$$w_{i,j} = w_{BCM_{i,j}} + w_{CS_{i,j}} \qquad \text{Eq. (14)}$$

BCM

The homeostatic component is based on a BCM-like plasticity. Our BCM is driven by two main equations:

$$\frac{dw_j}{dt} = \rho_{PF}\phi\left(\rho_{PC}, \theta_M\right) \qquad \text{Eq. (15)}$$

$$\frac{d\theta_M}{dt} = \left[\left(\rho_{PC}\right)^2 - \frac{\theta_M}{\tau_M}\right] \qquad \text{Eq. (16)}$$

where, ρ_k (where $k = PF, PC$), represents the instantaneous activity of the PF and the 200 ms average of the PC activity; θ_M is the moving threshold of the BCM and τ_M is the threshold time constant. This 200 ms window allows the BCM to include the effect of CSpk pauses on the average activity of the PC. Moreover, ϕ represents the general change in plasticity of the whole PC which is then modulated by ρ_{PF}:

$$\phi = \frac{\rho_{PC}(\rho_{PC} - \theta_M)}{\theta_M} \qquad \text{Eq. (17)}$$

This equation defines a parabola with zeros at $\rho_{PC} = 0, \theta_M$ and minimum equal to $\phi = -\frac{1}{4}\theta_M$ at $\rho_{PC} = \frac{1}{1}\theta_M$. We can see that, with this method, higher PC activity means a higher possible potentiation. We need to damp this so that we find that at lower ρ_{PC} we get both a higher possible potentiation and a much lower possible depression. The simplest way to flatten the curve is to add a hyperbolic factor with a shape constant $c = 0.01$ so that:

$$\frac{dw_{BCM_j}}{dt} = 5\rho_{PF}\, tanh\left(0.01\frac{\rho_{PC}(\rho_{PC} - \theta_M)}{\theta_M}\right) \qquad \text{Eq. (18)}$$

This BCM has the characteristics that we are looking for. The sliding threshold θ_M makes it homeostatic as the threshold depends on the activity of the PC, ρ_{PC}, inducing an equilibrium when average firing rate is roughly constant. When the PC fires more, θ_M increases and there is a higher probability of having depression (Fig. 2B). The same happens when the cell is firing less, then θ_M decreases in the direction of the PC activity, increasing the chances of potentiation.

LTD

The LTD is modeled as a negative change of the synaptic activity proportional to the activity of the PF and with a time decay of 350 ms (**Table 7**) simulating the calcium release time (**Fig. 2D**), where A_{CSpk} is the CSpk induced LTD constant.

$$\frac{dw_{CS_j}}{dt} = \frac{-w_{CS_j}}{\tau_{CSpk}} \qquad \text{Eq. (19)}$$

$$@IO\ spike\text{:}\ w_{CS_j} \mathrel{+}= A_{CSpk}\left|\rho_{PF_j} - I_{PF_0}\right| \qquad \text{Eq. (20)}$$

Table 7. Parameter values for the different micromodules

Zone	Coupling	Synaptic currents		Conductance	IO OU current parameters	
		CN to IO $\gamma^{(IO)}{}_{CN}$	PC to CN $\gamma^{(CN)}{}_{PC}$	g_{Cal}	$I^{(IO)}{}_{OU_0}$	$\sigma^{(IO)}{}_{OU}$
Upbound	Coupled	-2.0	0.005	1.2	-0.7	0.7
	Uncoupled	-2.0	0.005	1.4	-0.3	0.7
Downbound	Coupled	-1.8	0.004	1.4	-0.3	0.3
	Uncoupled	-1.8	0.004	1.4	-0.6	0.7

PC-CN Synapse

The inhibitory synapse from PC onto the CN is modeled by instantaneously increasing $I^{(CN)}{}_{PC}$ when there is a presynaptic PC spike. After $I^{(CN)}{}_{PC}$ is increased, the CN's frequency will be lower until $I^{(CN)}{}_{PC}$ decays back to $I^{(CN)}{}_{PC} = 0$.

$$\frac{dI^{(CN)}{}_{PC}}{dt} = \frac{-I^{(CN)}{}_{PC}}{\tau^{(CN)}{}_{PC}} \qquad \text{Eq. (21)}$$

$$@PC\ spike\text{:}\ I^{(CN)}{}_{PC} \mathrel{+}= \gamma^{(CN)}{}_{PC} \qquad \text{Eq. (22)}$$

Each PC projects to 16 CN cells and each CN cell receives on average from 40 PCs, ranging from 30 to 52 (**Fig. 1A**). Each PC source indices is repeated for each PC and CN target indices are sampled without replacement from the CN population.

CN-IO Synapse

Analogously to the PC-CN synapse, the new synaptic current $I^{(IO)}{}_{CN}$ increases with CN spikes. The decay time of $I^{(IO)}{}_{CN}$ is small (30 ms), and enters the IO at the soma ($I^{(s)}{}_{app}$). This inhibitory input can be seen as the asynchronous release of GABA into the IO cell [100]. The update value of $\gamma^{(IO)}{}_{CN}$ is seen in **Table 6** and the synaptic update is done as follows:

$$\frac{dI^{(IO)}{}_{CN}}{dt} = \frac{-I^{(IO)}{}_{CN}}{\tau^{(IO)}{}_{CN}} \qquad \text{Eq. (23)}$$

$$@CN\ spike\text{:}\ I^{(IO)}{}_{CN} \mathrel{+}= \frac{\gamma^{(IO)}{}_{CN}}{N_{CN}} \qquad \text{Eq. (24)}$$

Each CN projects to 10 IO cells and each IO cell receives on average from 10 CN cells, ranging from 6 to 16 (**Fig. 1A**). The connectivity is generated ensuring these ratios. CN cell indices are repeated for each CN cell, while IO indices are sampled without replacement from the IO population, avoiding duplicate connections.

IO-IO Gap Junction

The electrotonic coupling between the cells is represented by a current I_c (see **Table 6**) in the dendrites and the transjunctional voltage dependence of the gap junction conductance f [109] is defined below. In the coupled case, each IO neuron connects to all other neurons in the population (**Fig. 1A**).

$$I_c = g_c\left(V_d - V_{de}\right)f\left(V_d - V_{de}\right) \qquad \text{Eq. (25)}$$

$$f(V) = 0.6e^{\frac{V^2}{50^2}} + 0.4 \qquad \text{Eq. (26)}$$

IO-PC Synapse

The modeling of the IO-PC synapse focuses on the pause mechanism following a CSpk. Each PC receives a CF input from one IO as seen in **Fig. 1A**. As the PC AdEX model already has an adaptation variable *w* that increases the interspike interval (ISI), the synaptic modeling only requires the increase of *w* following a presynaptic IO spike. The update of the *w* adaptation variable is increased as shown in Eq 26. As *w* is increased to a higher value, the PC cannot spike until *w* decays to a lower value.

$$@IO\ spike\text{:}\ w^{PC} \mathrel{+}= \gamma^{(PC)}{}_{IO} \qquad \text{Eq. (27)}$$

Only half of the IOs synapse with PCs. Each of these IO CF connects to on average 5 PCs (ranging 2 to 9) and each PC receives from only 1 IO cell (**Fig. 1A**). IO cell indices are sampled without replacement from the IO population, ensuring each PC is either uniquely assigned to a source or connected to a randomly chosen source from the preselected pool.

Upbound and Downbound zones

To reproduce the physiological results of the different zones we did a grid search over 2 synaptic currents, 1 IO conductance and the IO OU current (see **Table 7**). This grid search was done in steps of 0.1 for all parameters except for the PC to CN synaptic current $\gamma^{(CN)}{}_{PC}$ which was done in steps of 0.001. Then we tried to find a set of parameters such that we could reproduce physiological firing ranges with minimal parameter changes between cases. **Table 7** shows the different parameters that need to be changed to reproduce electrophysiological results as shown in **Fig. 3**.

Filtered inputs

Filtered inputs were obtained via bandpass filtering. For each noise input and frequency range ($f_{c_{low}}$ to $f_{c_{high}}$), a forward 6th butterworth filter was applied on the mean-offset removed original noise signal, obtaining $y_{filtered}$. Filtering was done as cascaded second-order sections, taking into account sampling frequency as $\left(f_s = \frac{1}{dt}\right)$ with dt being the time step of the simulation. To account for power loss due to filtering, a correction was applied by multiplying the frequency-domain energy:

$$I_{PF_{filtered}} = y_{filtered} \frac{\sqrt{\Sigma\left|Y_{unfiltered}(f)\right|^2}}{\sqrt{\Sigma\left|Y_{filtered}(f)\right|^2}} + I_{PF_0} \qquad \text{Eq. (28)}$$

Simulations

For all simulations the Euler-Maruyama method was used to simulate the frozen noise. For the rest of the neuron groups, the forward Euler method was used to integrate the differential equations. Two integration timesteps were used, one for the simulations (0.025 ms) and one for the recording of the neuron output (1 ms). All experiments had a simulation length of 120 s. We first started by generating a seed which included generating a network with connectivities, cell parameters and frozen PF input. When modeling the different micromodules we used the parameters shown in **Table 7**.

The frozen PF input was used for the “no plasticity” experiment. Then, for the “plasticity” experiment we turned on the BCM and LTD mechanisms and we again gave the same exact frozen PF input. At the end of this experiment we filtered the weights using a Savitzky–Golay filter and then took the last value of that filtered weight. We chose this weight as the new static weight for the “after plasticity” experiment where we again gave as

input the same frozen input. This was continued in the same fashion for the second, third and fourth epochs of plasticity (see **Fig. 2G-L**).

The experiments with filtered signals were done in the same way. The only difference was that the new PF input was a filtered version of the same frozen input. We still had the same network seed. We redid the experiments for the following frequency bands: 5-10 Hz, 10-15 Hz, 15-20 Hz, 25-30 Hz, 50-75 Hz, 100-150 Hz and 1-800 Hz (see **Fig. 5A**).

For each of the simulations we also did a copy simulation with the uncoupled scenario. This is the same seed, meaning that we had the same network, same connectivity, same cell parameters, and same frozen PF input. The only difference was that the coupling conductance g_c (see Table 3) of the coupling current I_c is lowered to 0 ($g_c = 0$).

Acknowledgments

The authors would like to thank Laurens Bosman for his insights and comments on a previous version of the manuscript. We would also like to thank the NVIDIA corporation for supporting our research with the donation of 2 x RTX6000.

Author contributions

EF: Conceptualization, Investigation, Methodology, Writing – original draft, Writing – review & editing. LL: Methodology, Writing – original draft, Writing – review & editing. SH: Funding acquisition, Writing – review. CS: Funding acquisition, Writing – review. CDZ: Conceptualization, Funding acquisition, Investigation, Project administration, Resources, Supervision, Writing – original draft, Writing – review & editing. AB: Conceptualization, Funding acquisition, Investigation, Methodology, Project administration, Resources, Supervision, Writing – original draft, Writing – review & editing. MN: Conceptualization, Funding acquisition, Investigation, Methodology, Project administration, Resources, Supervision, Writing – original draft, Writing – review & editing.

Funding

This work was supported by the Netherlands Organization for Scientific Research (NWO) VIDI/917.18.380,2018/ZonMw (A.B), NWO NWA-ORC 2022 SCANNER (A.B), the Erasmus MC Convergence Health and Technology Integrative Neuromedicine Flagship Program (A.B. and M.N.), the 2021 H2020 funding (n°650003) (M.N). Financial support to CS provided by the European-Union Horizon Europe R&I program through projects SEPTON (no. 101094901) and SECURED (no. 101095717) and through the NWO - Gravitation Programme DBI2 (no. 024.005.022). Financial support to CIDZ was provided by the Netherlands Organization for Scientific Research (NWO-ALW 824.02.001), the Dutch Organization for Medical Sciences (ZonMW 91120067), Medical Neuro-Delta (MD 01092019-31082023), INTENSE LSH-NWO (TTW/00798883), ERC-adv (GA-294775) and ERC-POC (nrs. 737619 and 768914); The NIN Vriendenfonds for Albinism as well as the Dutch NWO Gravitation Program (DBI2).

Conflicts of interest

The authors declare that the research was conducted in the absence of any commercial or financial relationships that could be construed as a potential conflict of interest.

References

1. Zenke F, Gerstner W, Ganguli S. The temporal paradox of Hebbian learning and homeostatic plasticity. Curr Opin Neurobiol. 2017;43: 166–176.

2. Keck T, Hübener M, Bonhoeffer T. Interactions between synaptic homeostatic mechanisms: an attempt to reconcile BCM theory, synaptic scaling, and changing excitation/inhibition balance. Curr Opin Neurobiol. 2017;43: 87–93.

3. Hölzel RW, Krischer K. Stability and long term behavior of a Hebbian network of Kuramoto oscillators. SIAM J Appl Dyn Syst. 2015;14: 188–201.

4. Fernández Santoro EM, Karim A, Warnaar P, De Zeeuw CI, Badura A, Negrello M. Purkinje cell models: past, present and future. Front Comput Neurosci. 2024;18: 1426653.

5. De Zeeuw CI, Ten Brinke MM. Motor learning and the cerebellum. Cold Spring Harb Perspect Biol. 2015;7: a021683.

6. Heck D, Sultan F. Cerebellar structure and function: making sense of parallel fibers. Hum Mov Sci. 2002;21: 411–421.

7. Chaumont J, Guyon N, Valera AM, Dugué GP, Popa D, Marcaggi P, et al. Clusters of cerebellar Purkinje cells control their afferent climbing fiber discharge. Proc Natl Acad Sci U S A. 2013;110: 16223–16228.

8. De Zeeuw CI, Hoebeek FE, Bosman LWJ, Schonewille M, Witter L, Koekkoek SK. Spatiotemporal firing patterns in the cerebellum. Nat Rev Neurosci. 2011;12: 327–344.

9. Zhou H, Lin Z, Voges K, Ju C, Gao Z, Bosman LWJ, et al. Cerebellar modules operate at different frequencies. Elife. 2014;3: e02536.

10. Sudhakar SK, Hong S, Raikov I, Publio R, Lang C, Close T, et al. Spatiotemporal network coding of physiological mossy fiber inputs by the cerebellar granular layer. PLoS Comput Biol. 2017;13: e1005754.

11. Galliano E, Gao Z, Schonewille M, Todorov B, Simons E, Pop AS, et al. Silencing the majority of cerebellar granule cells uncovers their essential role in motor learning and consolidation. Cell Rep. 2013;3: 1239–1251.

12. Coesmans M, Weber JT, De Zeeuw CI, Hansel C. Bidirectional parallel fiber plasticity in the cerebellum under climbing fiber control. Neuron. 2004;44: 691–700.

13. Wang X, Novello M, Gao Z, Ruigrok TJH, De Zeeuw CI. Input and output organization of the mesodiencephalic junction for cerebro-cerebellar communication. J Neurosci Res. 2022;100: 620–637.

14. Kubo R, Aiba A, Hashimoto K. The anatomical pathway from the mesodiencephalic junction to the inferior olive relays perioral sensory signals to the cerebellum in the mouse. J Physiol. 2018;596: 3775–3791.

15. De Zeeuw CI, Simpson JI, Hoogenraad CC, Galjart N, Koekkoek SK, Ruigrok TJ. Microcircuitry and function of the inferior olive. Trends Neurosci. 1998;21: 391–400.

16. Loyola S, Hoogland TM, Hoedemaker H, Romano V, Negrello M, De Zeeuw CI. How inhibitory and excitatory inputs gate output of the inferior olive. Elife. 2023;12. doi:10.7554/eLife.83239

17. van Hoogstraten WS, Lute MCC, Liu Z, Broersen R, Mangili L, Kros L, et al. Disynaptic inhibitory cerebellar control over caudal medial accessory Olive. eNeuro. 2024;11: ENEURO.0262–23.2023.

18. Wang X, Liu Z, Angelov M, Feng Z, Li X, Li A, et al. Excitatory nucleo-olivary pathway shapes cerebellar outputs for motor control. Nat Neurosci. 2023;26: 1394–1406.

19. Broersen R, De Zeeuw CI. Keeping track of time: An interaction of mossy fibers and climbing fibers. Neuron. 2024;112: 2664–2666.

20. Gao Z, van Beugen BJ, De Zeeuw CI. Distributed synergistic plasticity and cerebellar learning. Nat Rev Neurosci. 2012;13: 619–635.

21. Lisman J. Long-term potentiation: outstanding questions and attempted synthesis. Long-term Potentiation: Enhancing Neuroscience for 30 years. Oxford University PressOxford; 2004. pp. 371–392.

22. Allen CB, Celikel T, Feldman DE. Long-term depression induced by sensory deprivation during cortical map plasticity in vivo. Nat Neurosci. 2003;6: 291–299.

23. Abbott LF, Nelson SB. Synaptic plasticity: taming the beast. Nat Neurosci. 2000;3 Suppl: 1178–1183.

24. Ito M. Mechanisms of motor learning in the cerebellum. Brain Res. 2000;886: 237–245.

25. Gutierrez-Castellanos N, Da Silva-Matos CM, Zhou K, Canto CB, Renner MC, Koene LMC, et al. Motor Learning Requires Purkinje Cell Synaptic Potentiation through Activation of AMPA-Receptor Subunit GluA3. Neuron. 2017;93: 409–424.

26. Suvrathan A, Raymond JL. Depressed by learning-heterogeneity of the plasticity rules at parallel fiber synapses onto Purkinje cells. Cerebellum. 2018;17: 747–755.

27. De Zeeuw CI, Lisberger SG, Raymond JL. Diversity and dynamism in the cerebellum. Nat Neurosci. 2021;24: 160–167.

28. De Zeeuw CI. Bidirectional learning in upbound and downbound microzones of the cerebellum. Nat Rev Neurosci. 2021;22: 92–110.

29. Llinas R, Baker R, Sotelo C. Electrotonic coupling between neurons in cat inferior olive. J Neurophysiol. 1974;37: 560–571.

30. Sotelo C, Llinas R, Baker R. Structural study of inferior olivary nucleus of the cat: morphological correlates of electrotonic coupling. J Neurophysiol. 1974;37: 541–559.

31. De Zeeuw CI, Lang EJ, Sugihara I, Ruigrok TJ, Eisenman LM, Mugnaini E, et al. Morphological correlates of bilateral synchrony in the rat cerebellar cortex. J Neurosci. 1996;16: 3412–3426.

32. Llinás R, Yarom Y. Properties and distribution of ionic conductances generating electroresponsiveness of mammalian inferior olivary neurones in vitro. J Physiol. 1981;315: 569–584.

33. Leznik E, Llinás R. Role of gap junctions in synchronized neuronal oscillations in the inferior olive. J Neurophysiol. 2005;94: 2447–2456.

34. Bazzigaluppi P, Ruigrok T, Saisan P, De Zeeuw CI, de Jeu M. Properties of the nucleo-olivary pathway: an in vivo whole-cell patch clamp study. PLoS One. 2012;7: e46360.

35. Negrello M, Warnaar P, Romano V, Owens CB, Lindeman S, Iavarone E, et al. Quasiperiodic rhythms of the inferior olive. PLoS Comput Biol. 2019;15: e1006475.

36. Khosrovani S, Van Der Giessen RS, De Zeeuw CI, De Jeu MTG. In vivo mouse inferior olive neurons exhibit heterogeneous subthreshold oscillations and spiking patterns. Proc Natl Acad Sci U S A. 2007;104: 15911–15916.

37. de Zeeuw CI, Holstege JC, Ruigrok TJ, Voogd J. Ultrastructural study of the GABAergic, cerebellar, and mesodiencephalic innervation of the cat medial accessory olive: anterograde tracing combined with immunocytochemistry. J Comp Neurol. 1989;284: 12–35.

38. de Zeeuw CI, Ruigrok TJ, Holstege JC, Jansen HG, Voogd J. Intracellular labeling of neurons in the medial accessory olive of the cat: II. Ultrastructure of dendritic spines and their GABAergic innervation. J Comp Neurol. 1990;300: 478–494.

39. Rall W, Segev I. Space-clamp problems when voltage clamping branched neurons with intracellular microelectrodes. Voltage and Patch Clamping with Microelectrodes. New York, NY: Springer New York; 1985. pp. 191–215.

40. Chen X, Kovalchuk Y, Adelsberger H, Henning HA, Sausbier M, Wietzorrek G, et al. Disruption of the olivo-cerebellar circuit by Purkinje neuron-specific ablation of BK channels. Proc Natl Acad Sci U S A. 2010;107: 12323–12328.

41. De Gruijl JR, Sokol PA, Negrello M, De Zeeuw CI. Modulation of electrotonic coupling in the inferior Olive by inhibitory and excitatory inputs: Integration in the glomerulus. bioRxiv. bioRxiv; 2016. doi:10.1101/072041

42. Lefler Y, Torben-Nielsen B, Yarom Y. Oscillatory activity, phase differences, and phase resetting in the inferior olivary nucleus. Front Syst Neurosci. 2013;7: 22.

43. Shimizu G, Yoshida K, Kasai H, Toyoizumi T. Computational roles of intrinsic synaptic dynamics. bioRxiv. bioRxiv; 2021. doi:10.1101/2021.04.22.441034

44. Sussillo D, Toyoizumi T, Maass W. Self-tuning of neural circuits through short-term synaptic plasticity. J Neurophysiol. 2007;97: 4079–4095.

45. Canolty RT, Ganguly K, Kennerley SW, Cadieu CF, Koepsell K, Wallis JD, et al. Oscillatory phase coupling coordinates anatomically dispersed functional cell assemblies. Proc Natl Acad Sci U S A. 2010;107: 17356–17361.

46. Molter C, Salihoglu U, Bersini H. The road to chaos by time-asymmetric Hebbian learning in recurrent neural networks. Neural Comput. 2007;19: 80–110.

47. Rabinowitch I, Segev I. Two opposing plasticity mechanisms pulling a single synapse. Trends Neurosci. 2008;31: 377–383.

48. van Rossum MC, Bi GQ, Turrigiano GG. Stable Hebbian learning from spike timing-dependent plasticity. J Neurosci. 2000;20: 8812–8821.

49. Voogd J, Glickstein M. The anatomy of the cerebellum. Trends Neurosci. 1998;21: 370–375.

50. Hoang H, Tsutsumi S, Matsuzaki M, Kano M, Kawato M, Kitamura K, et al. Dynamic organization of cerebellar climbing fiber response and synchrony in multiple functional components reduces dimensions for reinforcement learning. Elife. 2023;12: e86340.

51. Zhang J, Tran-Anh K, Hirata T, Sugihara I. Striped distribution pattern of Purkinje cells of different birthdates in the mouse cerebellar cortex studied with the Neurog2-CreER transgenic

line. Neuroscience. 2021;462: 122–140.

52. Voogd J, Ruigrok TJH. The organization of the corticonuclear and olivocerebellar climbing fiber projections to the rat cerebellar vermis: the congruence of projection zones and the zebrin pattern. J Neurocytol. 2004;33: 5–21.

53. Chen X, Du Y, Broussard GJ, Kislin M, Yuede CM, Zhang S, et al. Transcriptomic mapping uncovers Purkinje neuron plasticity driving learning. Nature. 2022;605: 722–727.

54. Voerman S, Urbanus BHA, Schonewille M, White JJ, De Zeeuw CI. Postsynaptic plasticity of Purkinje cells in mice is determined by molecular identity. Commun Biol. 2022;5: 1328.

55. de Solages C, Szapiro G, Brunel N, Hakim V, Isope P, Buisseret P, et al. High-frequency organization and synchrony of activity in the purkinje cell layer of the cerebellum. Neuron. 2008;58: 775–788.

56. Kistler WM. Time-slicing: A model for cerebellar function based on synchronization, reverberation, and time windows. Neurocomputing. 2001;38-40: 1367–1372.

57. Ju C, Bosman LWJ, Hoogland TM, Velauthapillai A, Murugesan P, Warnaar P, et al. Neurons of the inferior olive respond to broad classes of sensory input while subject to homeostatic control. J Physiol. 2019;597: 2483–2514.

58. Warnaar P, Couto J, Negrello M, Junker M, Smilgin A, Ignashchenkova A, et al. Duration of Purkinje cell complex spikes increases with their firing frequency. Front Cell Neurosci. 2015;9: 122.

59. Devor A, Yarom Y. Coherence of subthreshold activity in coupled inferior olivary neurons. Ann N Y Acad Sci. 2002;978: 508.

60. Jacobson GA, Lev I, Yarom Y, Cohen D. Invariant phase structure of olivo-cerebellar oscillations and its putative role in temporal pattern generation. Proc Natl Acad Sci U S A. 2009;106: 3579–3584.

61. Lampl I, Yarom Y. Subthreshold oscillations and resonant behavior: two manifestations of the same mechanism. Neuroscience. 1997;78: 325–341.

62. Torben-Nielsen B, Segev I, Yarom Y. The generation of phase differences and frequency changes in a network model of inferior olive subthreshold oscillations. PLoS Comput Biol. 2012;8: e1002580.

63. Yarom Y. Rhythmogenesis in a hybrid system--interconnecting an olivary neuron to an analog network of coupled oscillators. Neuroscience. 1991;44: 263–275.

64. Lanore F, Cayco-Gajic NA, Gurnani H, Coyle D, Silver RA. Cerebellar granule cell axons support high-dimensional representations. Nat Neurosci. 2021;24: 1142–1150.

65. Badura A, De Zeeuw CI. Cerebellar granule cells: Dense, rich and evolving representations. Curr Biol. 2017;27: R415–R418.

66. Uhlenbeck GE, Ornstein LS. On the theory of the Brownian motion. Phys Rev. 1930;36: 823–841.

67. Sultan F. Distribution of mossy fibre rosettes in the cerebellum of cat and mice: evidence for a parasagittal organization at the single fibre level. Eur J Neurosci. 2001;13: 2123–2130.

68. Isope P, Barbour B. Properties of unitary granule cell-->Purkinje cell synapses in adult rat

cerebellar slices. J Neurosci. 2002;22: 9668–9678.

69. Abbasi S, Hudson AE, Maran SK, Cao Y, Abbasi A, Heck DH, et al. Robust transmission of rate coding in the inhibitory Purkinje cell to cerebellar nuclei pathway in awake mice. PLoS Comput Biol. 2017;13: e1005578.

70. Najac M, Raman IM. Integration of Purkinje cell inhibition by cerebellar nucleo-olivary neurons. J Neurosci. 2015;35: 544–549.

71. Van Der Giessen RS, Koekkoek SK, van Dorp S, De Gruijl JR, Cupido A, Khosrovani S, et al. Role of olivary electrical coupling in cerebellar motor learning. Neuron. 2008;58: 599–612.

72. Kølvraa M, Müller FC, Jahnsen H, Rekling JC. Mechanisms contributing to cluster formation in the inferior olivary nucleus in brainstem slices from postnatal mice. J Physiol. 2014;592: 33–47.

73. Vrieler N, Loyola S, Yarden-Rabinowitz Y, Hoogendorp J, Medvedev N, Hoogland TM, et al. Variability and directionality of inferior olive neuron dendrites revealed by detailed 3D characterization of an extensive morphological library. Brain Struct Funct. 2019;224: 1677–1695.

74. ten Brinke MM, Boele H-J, Spanke JK, Potters J-W, Kornysheva K, Wulff P, et al. Evolving models of Pavlovian conditioning: Cerebellar cortical dynamics in awake behaving mice. Cell Rep. 2015;13: 1977–1988.

75. Cook AA, Fields E, Watt AJ. Losing the Beat: Contribution of Purkinje Cell Firing Dysfunction to Disease, and Its Reversal. Neuroscience. 2021;462: 247–261.

76. Geminiani A, Casellato C, Boele H-J, Pedrocchi A, De Zeeuw CI, D'Angelo E. Mesoscale simulations predict the role of synergistic cerebellar plasticity during classical eyeblink conditioning. PLoS Comput Biol. 2024;20: e1011277.

77. Witter L, Canto CB, Hoogland TM, de Gruijl JR, De Zeeuw CI. Strength and timing of motor responses mediated by rebound firing in the cerebellar nuclei after Purkinje cell activation. Front Neural Circuits. 2013;7: 133.

78. Hoebeek FE, Witter L, Ruigrok TJH, De Zeeuw CI. Differential olivo-cerebellar cortical control of rebound activity in the cerebellar nuclei. Proc Natl Acad Sci U S A. 2010;107: 8410–8415.

79. Romano V, Reddington AL, Cazzanelli S, Mazza R, Ma Y, Strydis C, et al. Functional convergence of autonomic and sensorimotor processing in the lateral cerebellum. Cell Rep. 2020;32: 107867.

80. Yamazaki T, Lennon W. Revisiting a theory of cerebellar cortex. Neurosci Res. 2019;148: 1–8.

81. D'Angelo E. Challenging Marr's theory of the cerebellum. Computational Theories and their Implementation in the Brain. Oxford University Press; 2016. pp. 62–78.

82. Kawato M, Furukawa K, Suzuki R. A hierarchical neural-network model for control and learning of voluntary movement. Biol Cybern. 1987;57: 169–185.

83. Raymond JL, Lisberger SG, Mauk MD. The cerebellum: a neuronal learning machine? Science. 1996;272: 1126–1131.

84. Barto AG, Fagg AH, Sitkoff N, Houk JC. A cerebellar model of timing and prediction in the control of reaching. Neural Comput. 1999;11: 565–594.

85. Medina JF, Mauk MD. Computer simulation of cerebellar information processing. Nat Neurosci. 2000;3 Suppl: 1205–1211.

86. Herzfeld DJ, Kojima Y, Soetedjo R, Shadmehr R. Encoding of error and learning to correct that error by the Purkinje cells of the cerebellum. Nat Neurosci. 2018;21: 736–743.

87. Glaser JI, Benjamin AS, Farhoodi R, Kording KP. The roles of supervised machine learning in systems neuroscience. Prog Neurobiol. 2019;175: 126–137.

88. Manto M, Bower JM, Conforto AB, Delgado-García JM, da Guarda SNF, Gerwig M, et al. Consensus paper: roles of the cerebellum in motor control--the diversity of ideas on cerebellar involvement in movement. Cerebellum. 2012;11: 457–487.

89. Hong S, Negrello M, Junker M, Smilgin A, Thier P, De Schutter E. Multiplexed coding by cerebellar Purkinje neurons. Elife. 2016;5. doi:10.7554/eLife.13810

90. Braitenberg V. In defense of the cerebellum. Ann N Y Acad Sci. 2002;978: 175–183.

91. Oja E. A simplified neuron model as a principal component analyzer. J Math Biol. 1982;15: 267–273.

92. Brito CSN, Gerstner W. Nonlinear Hebbian learning as a unifying principle in receptive field formation. PLoS Comput Biol. 2016;12: e1005070.

93. Voerman S, Broersen R, Swagemakers SMA, De Zeeuw CI, van der Spek PJ. Plasticity mechanisms of genetically distinct Purkinje cells. Bioessays. 2024;46: e2400008.

94. Rodriques SG, Stickels RR, Goeva A, Martin CA, Murray E, Vanderburg CR, et al. Slide-seq: A scalable technology for measuring genome-wide expression at high spatial resolution. Science. 2019;363: 1463–1467.

95. Hao S, Zhu X, Huang Z, Yang Q, Liu H, Wu Y, et al. Cross-species single-cell spatial transcriptomic atlases of the cerebellar cortex. Science. 2024;385: eado3927.

96. Bina L, Romano V, Hoogland TM, Bosman LWJ, De Zeeuw CI. Purkinje cells translate subjective salience into readiness to act and choice performance. Cell Rep. 2021;37: 110116.

97. Solinas S, Nieus T, D'Angelo E. A realistic large-scale model of the cerebellum granular layer predicts circuit spatio-temporal filtering properties. Front Cell Neurosci. 2010;4: 12.

98. Wulff P, Schonewille M, Renzi M, Viltono L, Sassoe-Pognetto M, Badura A, et al. Synaptic inhibition of Purkinje cells mediates consolidation of vestibulo-cerebellar motor learning. Nat Neurosci. 2009;12: 1042–1049.

99. Badura A, Schonewille M, Voges K, Galliano E, Renier N, Gao Z, et al. Climbing fiber input shapes reciprocity of Purkinje cell firing. Neuron. 2013;78: 700–713.

100. Best AR, Regehr WG. Inhibitory regulation of electrically coupled neurons in the inferior olive is mediated by asynchronous release of GABA. Neuron. 2009;62: 555–565.

101. Andersson G, Hesslow G. Activity of Purkinje cells and interpositus neurones during and after periods of high frequency climbing fibre activation in the cat. Exp Brain Res. 1987;67: 533–542.

102. Caligiore D, Pezzulo G, Baldassarre G, Bostan AC, Strick PL, Doya K, et al. Consensus paper: Towards a systems-level view of cerebellar function: The interplay between cerebellum, basal ganglia, and cortex. Cerebellum. 2017;16: 203–229.

103. Lefler Y, Yarom Y, Uusisaari MY. Cerebellar inhibitory input to the inferior olive decreases electrical coupling and blocks subthreshold oscillations. Neuron. 2014;81: 1389–1400.

104. Bauer S, van Wingerden N, Jacobs T, van der Horst A, Zhai P, Betting J-HLF, et al. Purkinje cell activity resonation generates rhythmic behaviors at the preferred frequency of 8 Hz. Biomedicines. 2022;10: 1831.

105. Brette R, Gerstner W. Adaptive exponential integrate-and-fire model as an effective description of neuronal activity. J Neurophysiol. 2005;94: 3637–3642.

106. Goodman D, Brette R. Brian: a simulator for spiking neural networks in python. Front Neuroinform. 2008;2: 5.

107. Abbott LF, Dayan P. Theoretical neuroscience. In: MIT Press [Internet]. The MIT Press, Massachusetts Institute of Technology; 1 Dec 2021 [cited 2 Sep 2024]. Available: https://mitpress.mit.edu/9780262041997/theoretical-neuroscience/

108. De Gruijl JR, Bazzigaluppi P, de Jeu MTG, De Zeeuw CI. Climbing fiber burst size and olivary sub-threshold oscillations in a network setting. PLoS Comput Biol. 2012;8: e1002814.

109. Schweighofer N, Doya K, Kawato M. Electrophysiological properties of inferior olive neurons: A compartmental model. J Neurophysiol. 1999;82: 804–817.

110. Llinás R, Yarom Y. Electrophysiology of mammalian inferior olivary neurones in vitro. Different types of voltage-dependent ionic conductances. J Physiol. 1981;315: 549–567.

111. Bal T, McCormick DA. Synchronized oscillations in the inferior olive are controlled by the hyperpolarization-activated cation current I(h). J Neurophysiol. 1997;77: 3145–3156.

112. Ruigrok TJH, Voogd J. Cerebellar influence on olivary excitability in the cat. Eur J Neurosci. 1995;7: 679–693.

113. Hesslow G. Inhibition of inferior olivary transmission by mesencephalic stimulation in the cat. Neurosci Lett. 1986;63: 76–80.

114. Andersson G, Hesslow G. Inferior olive excitability after high frequency climbing fibre activation in the cat. Exp Brain Res. 1987;67: 523–532.

115. Andersson G, Oscarsson O. Projections to lateral vestibular nucleus from cerebellar climbing fiber zones. Exp Brain Res. 1978;32: 549–564.

116. Bienenstock EL, Cooper LN, Munro PW. Theory for the development of neuron selectivity: orientation specificity and binocular interaction in visual cortex. J Neurosci. 1982;2: 32–48.

117. McInnes L, Healy J, Astels S. hdbscan: Hierarchical density based clustering. J Open Source Softw. 2017;2: 205.

Supplementary Material

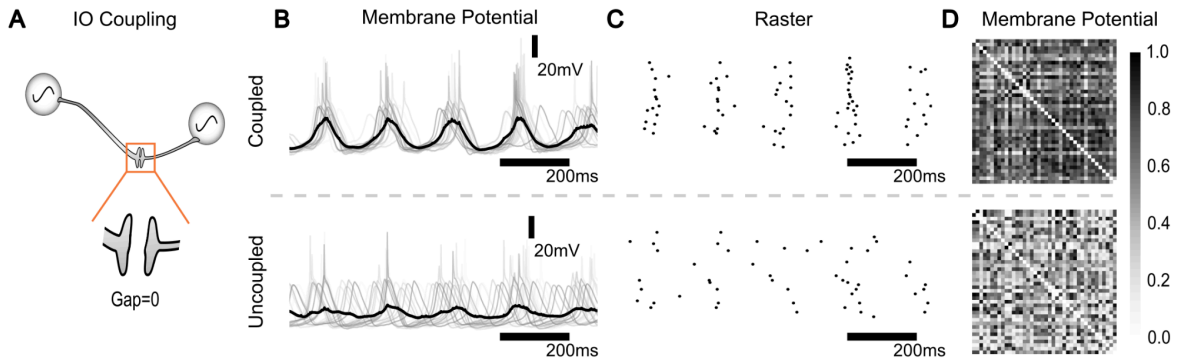

Supplementary Figure S1. Gap junctions increase spiking and subthreshold synchrony (A) *Gap junctions are disabled by setting the gap junction current = 0. For the Downbound micromodule, we compare the IO membrane response* ***(B)****, raster* ***(C)****, and correlation matrix of membrane potentials* ***(D)*** *in coupled (top) and uncoupled networks (bottom). Synchrony directly impacts the correlations in weight changes expected at the PF-PC synapse.*

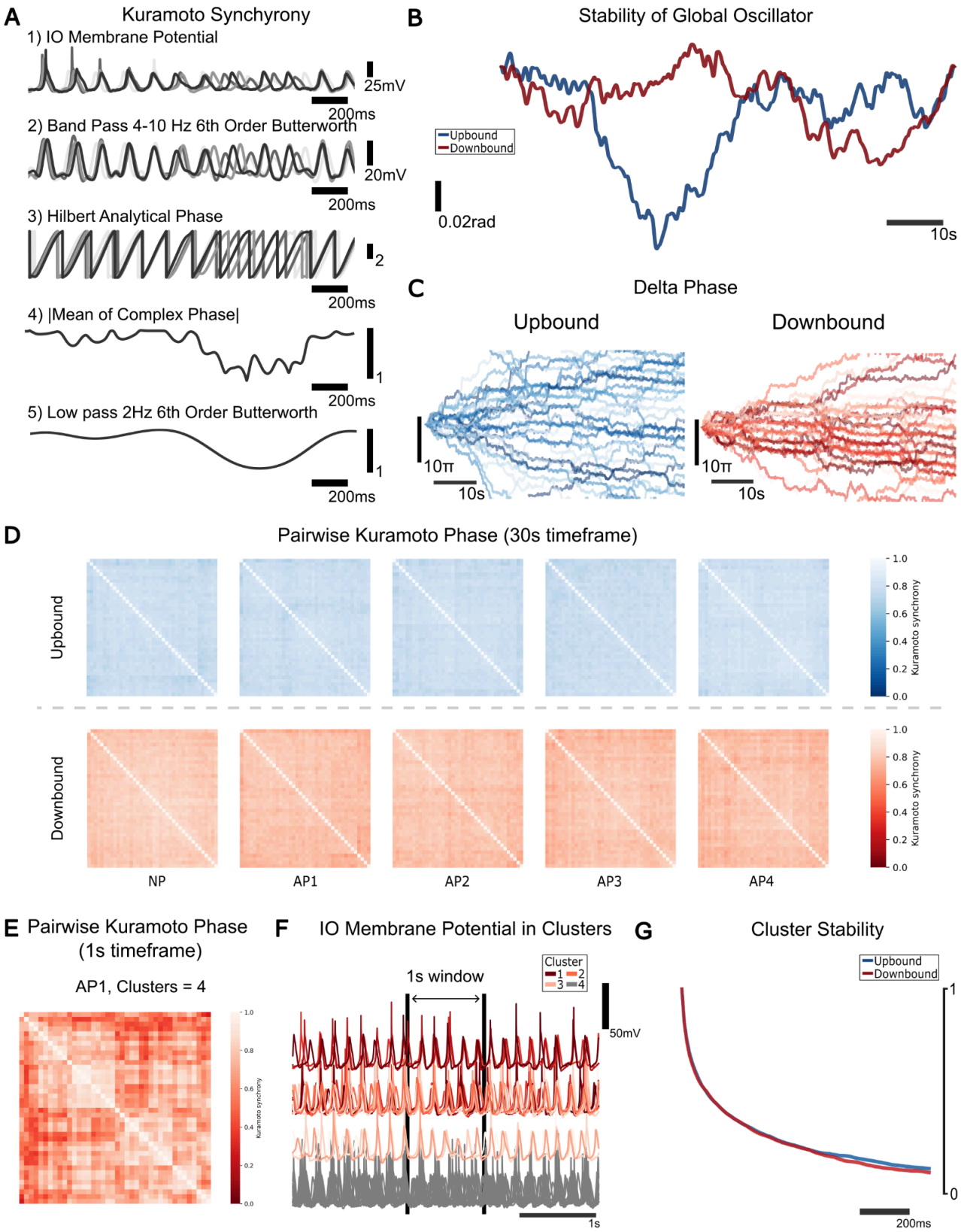

Supplementary Figure S2-1. Synchrony and Clustering. *In a single micromodule we observe a few clusters in the short time scale whose stability fades exponentially.* ***(A)*** *Kuramoto synchrony metric for STOs is derived from IO Vm in 5 transformation steps.* ***(B)*** *Stability of global oscillator (i.e. usability as a low dimensional global clock): global phase (mean Hilbert phase of all IO cells) from start to end of an 80 second period. The deviation*

from horizontal indicates phase drifts across phase in radians. Both Upbound and Downbound IO have small drifts and maintain a robust global phase, equating with a single synchronized cluster. ***(C)*** *Delta phase plot. Difference of phase of each IO neuron to the global phase over time. Plotted modulo 32pi radians to preserve space. Phase-locked oscillators are clearly visible as overlapping lines, while lag/leap events are shown as vertical jumps. Comparing long (****D,*** *30s) and short term (****E,*** *1s) clusterization with the pairwise kuramoto phase reveals a few clusters but a single global oscillator in the 30s frame.* ***(F)*** *Voltage trace of the clusters found in* ***E****. The black bars indicate the 1s used for clustering.* ***(G)*** *Cluster stability of 1s clusters. In intervals of 10ms, 1s clusters were found with HDBSCAN [117] and compared with each other via NMI (normalized mutual information). At a distance of 1s, clusters are barely related.*

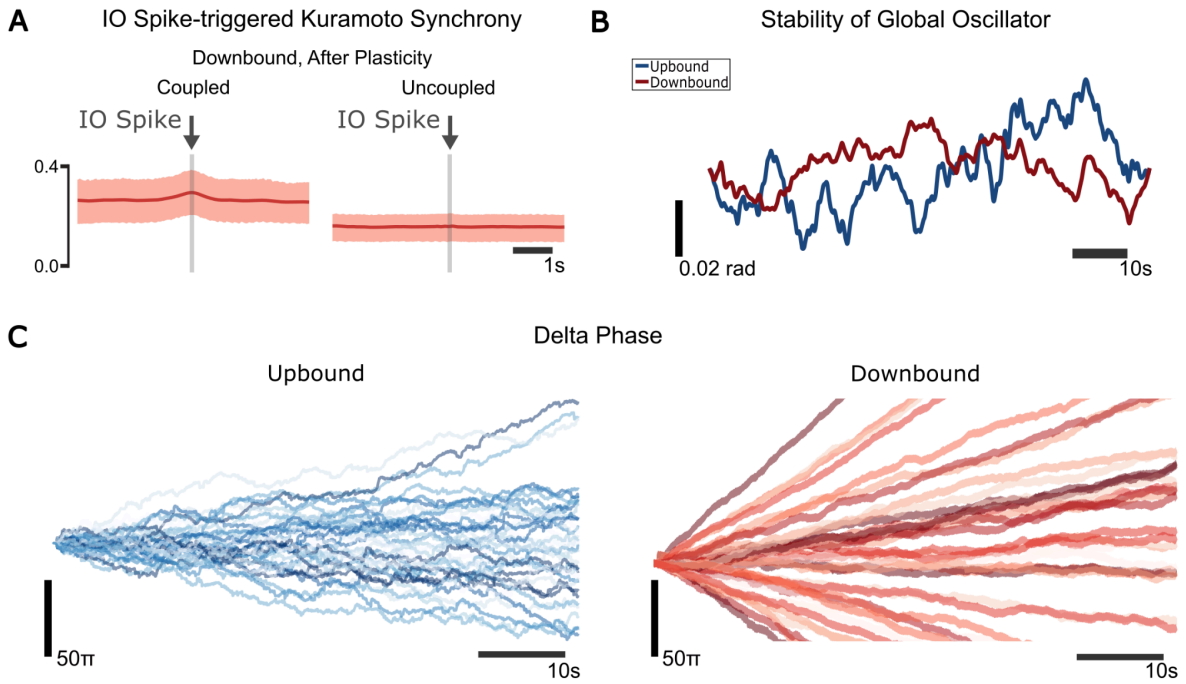

Supplementary Figure S2-2. Uncoupled Synchrony. *When uncoupled, the global oscillator still exhibits stable clock behavior. In Upbound zones there is less phase dispersion, but no phase locking appears in uncoupled scenarios. Downbound zone oscillators act completely independently.* ***(A)*** *IO Spike triggered Kuramoto synchrony with average 25/75 percentiles in Downbound, after plasticity. Average STO synchrony is higher for the coupled case. STO synchrony peaks before and after IO spikes in the coupled case, but not for the uncoupled case. This indicates that gap junctions not only set a base level of synchrony, but they also induce synchronous spikes. Note the increase of synchrony before the IO spike in the coupled case.* ***(B)*** *Stability of the global oscillator (see S2.1B), for the uncoupled case. Mean oscillator phase has smaller variation.* ***(C)*** *Delta phase plot (see S2.1C) for the uncoupled case (without modulo because phase locking does not occur as in the coupled case (Figure S2-1). IO neurons in the Upbound zone still keep some synchrony while for Downbound zones, oscillators behave independently.*

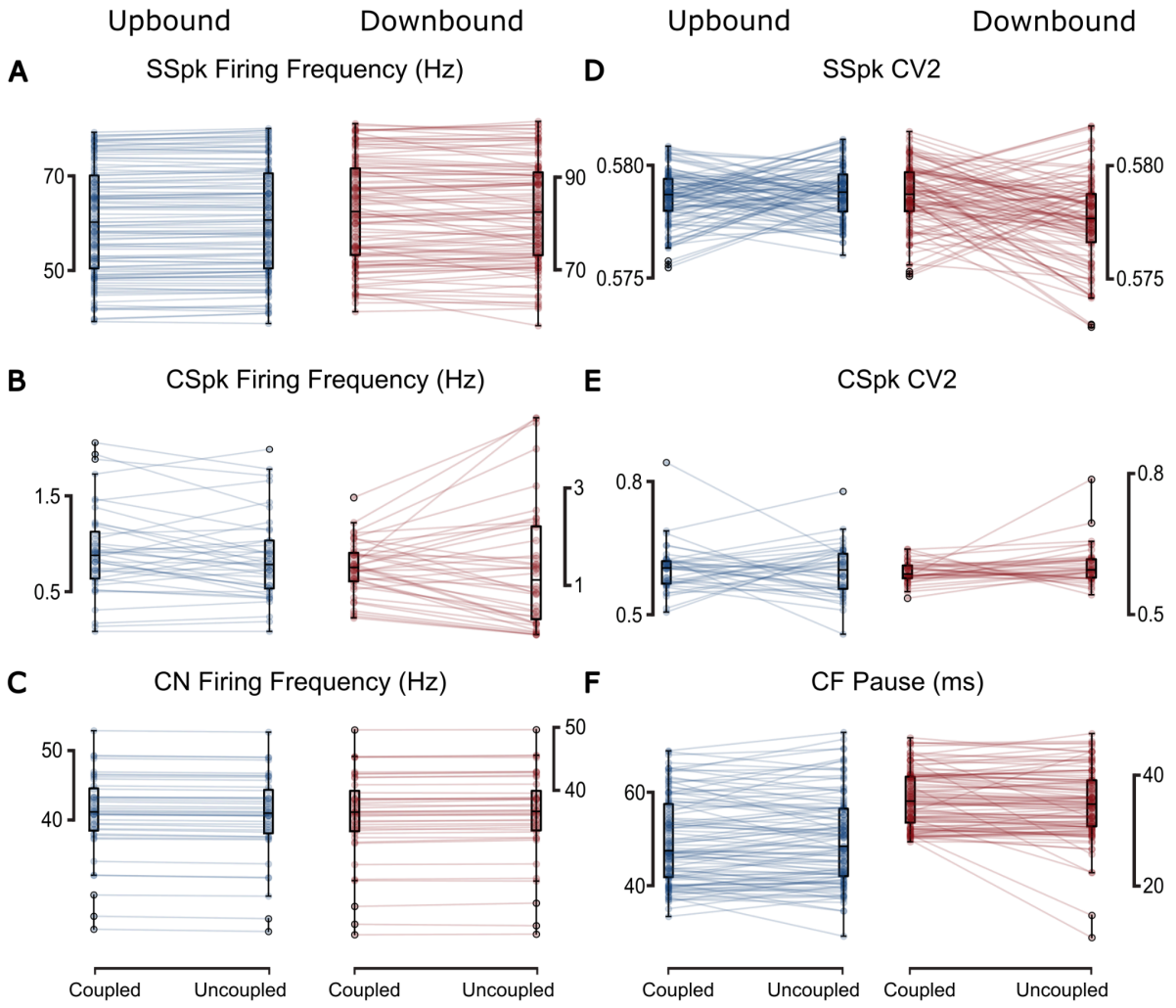

Supplementary Figure S3 Difference between coupled and uncoupled scenarios. (A) *SSpks frequency is significantly different across zones (coupled:* ***t=13.9, p<0.001****, uncoupled:* ***t=13.61, p<0.001; two-sample Student's t-test****).* ***(B)*** *CSpks frequency (coupled:* ***t=3.98, p<0.001****, uncoupled:* ***t=2.5, p=0.014; two-sample Student's t-test****). The variance of CSpks is significantly different in the uncoupled case across zones(****F=8.65, p<0.001; F-test using CCDF of F-distribution****).* ***(C)*** *The CN firing frequency (coupled:* ***t=-3.26, p=0.002****, uncoupled:* ***t=-2.98, p=0.004; two-sample Student's t-test****).* ***(D)*** *SSpk CV2 is significantly different for the Downbound zone across coupling cases (****t=4.50, p<0.001; two-sample Student's t-test****). For the uncoupled case, across both zones, the SSpk CV2 is significantly different (****t=-4.86, p<0.001; two-sample Student's t-test****) as well as the variance (****F=2.52, p<0.001; F-test using CCDF of F-distribution****).* ***(E)*** *CSpk CV2 boxplots.* ***(F)*** *The length of the CF Pause is significantly different across zones for both coupling cases (coupled:* ***t=-12.52, p<0.001****, uncoupled:* ***t=-14.39, p=0.014; two-sample Student's t-test****).*

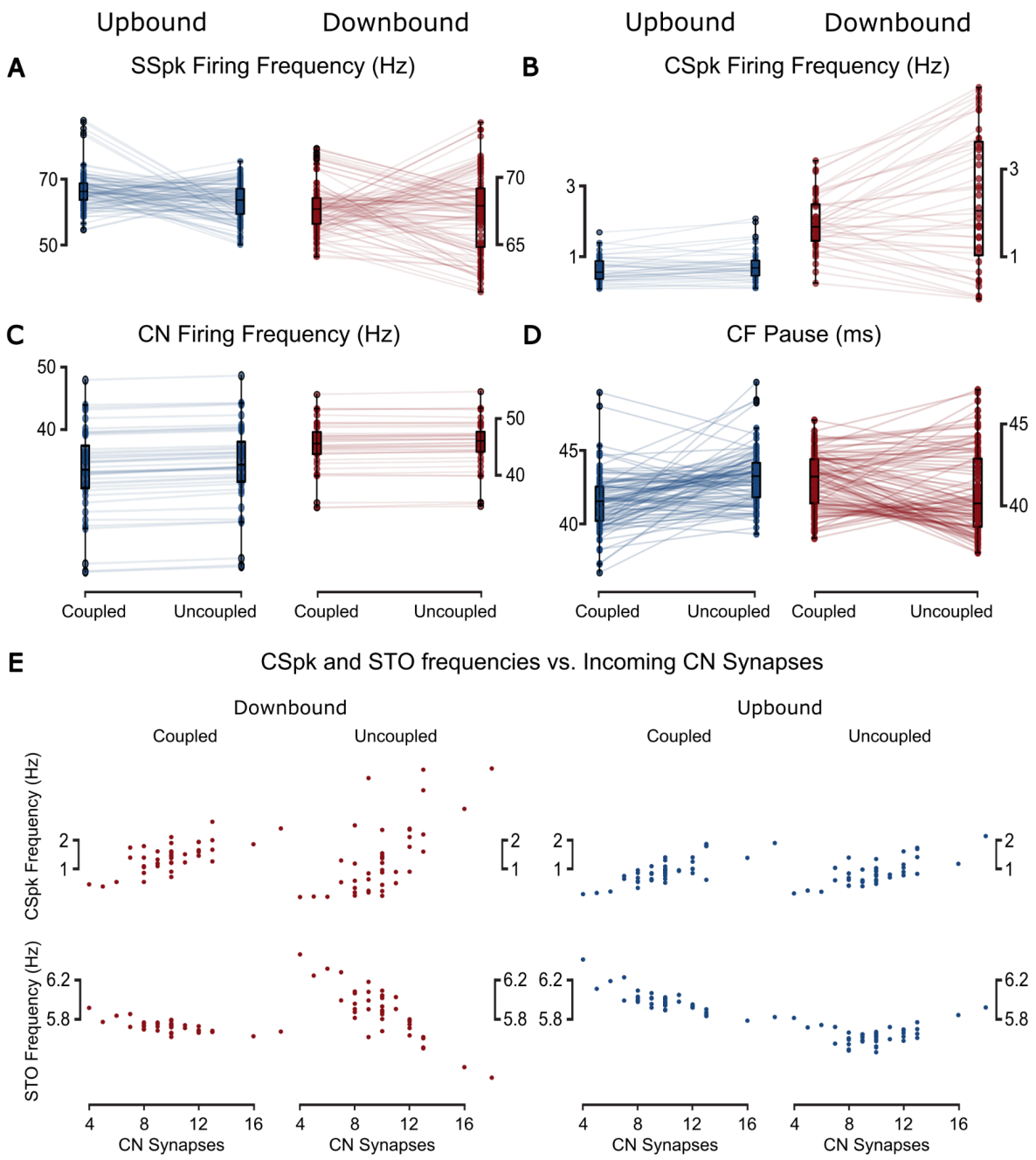

Supplementary Figure S4 More CN inhibition leads to less STO frequency and to more CSpk frequency. (A) *After Plasticity difference for SSpks is significant across coupled cases for the Upbound zone (**t=4.51, p<0.001; two-sample Student's t-test**) and for coupled case across zones (**t=-5.36, p<0.001; two-sample Student's t-test**). The variance of SSpk frequency is significantly different for the coupled case across both zones (**F=4.85, p<0.001; F-test using CCDF of F-distribution**). **(B)** CSpk frequency is significantly different across coupling cases (coupled: **t=9.44, p<0.001**, uncoupled: **t=5.84, p<0.001; two-sample Student's t-test**) and the variance is also significantly different (coupled: **F=2.91, p<0.001**, uncoupled: **F=12.19, p<0.001; F-test using CCDF of F-distribution**). **(C)** CN firing frequency is significantly different across coupling cases (coupled: **t=9.15, p<0.001**, uncoupled: **t=8.87, p<0.001; two-sample Student's t-test**). **(D)** The length of the CF pause is significantly different across coupling cases for Upbound and Downbound zones (Upbound: **t=-6.25, p<0.001**, Downbound: **t=2.5, p=0.013; two-sample Student's t-test**). It is also significantly different across zones for the uncoupled case (**t=-7.76, p<0.001; two-sample Student's t-test**).*

Supplementary Table S1 - PC SSpk frequency statistics

	Difference compared to NF Upbound		Difference compared to NF Downbound		Across Upbound and Downbound
	two-sample Student's t-test	two-sample ks-test	two-sample Student's t-test	two-sample ks-test	two-sample ks-test
NF	**-**	**-**	**-**	**-**	***D=0.48, p<0.001***
5-10	***t=8.18, p<0.001***	***D=0.62, p<0.001***	***t=10.29, p<0.001***	***D=0.72, p<0.001***	***D=0.54, p<0.001***
10-15	***t=11.98, p<0.001***	***D=0.74, p<0.001***	***t=11.81, p<0.001***	***D=0.68, p<0.001***	***D=0.70, p<0.001***
25-30	***t=13.7, p<0.001***	***D=0.77, p<0.001***	*p>0.05*	*p>0.05*	***D=0.55, p<0.001***
50-75	***t=12.56, p<0.001***	***D=0.70, p<0.001***	*p>0.05*	*p>0.05*	***D=0.3, p<0.001***
100-150	***t=11.81, p<0.001***	***D=0.74, p<0.001***	***t=6.5, p<0.001***	***D=0.46, p<0.001***	***D=0.38, p<0.001***
1-800	***t=10.2, p<0.001***	***D=0.67, p<0.001***	***t=5.66, p<0.001***	***D=0.32, p<0.001***	***D=0.21, p=0.024***

Supplementary Table S2 - CN and IO spike frequency statistics across Upbound and Downbound modules

	CN	IO
	two-sample ks-test	two-sample ks-test
NF	***D=0.78, p<0.001***	***D=0.78, p<0.001***
5-10	***D=0.80, p<0.001***	***D=0.53, p<0.001***
10-15	***D=0.78, p<0.001***	***D=0.78, p<0.001***
25-30	***D=0.72, p<0.001***	***D=0.82, p<0.001***
50-75	***D=0.72, p<0.001***	***D=0.80, p<0.001***
100-150	***D=0.75, p<0.001***	***D=0.82, p<0.001***
1-800	***D=0.75, p<0.001***	***D=0.70, p<0.001***